JHU/APL
SIR 79U-019
AUGUST 1979
REVISED
JANUARY 1980

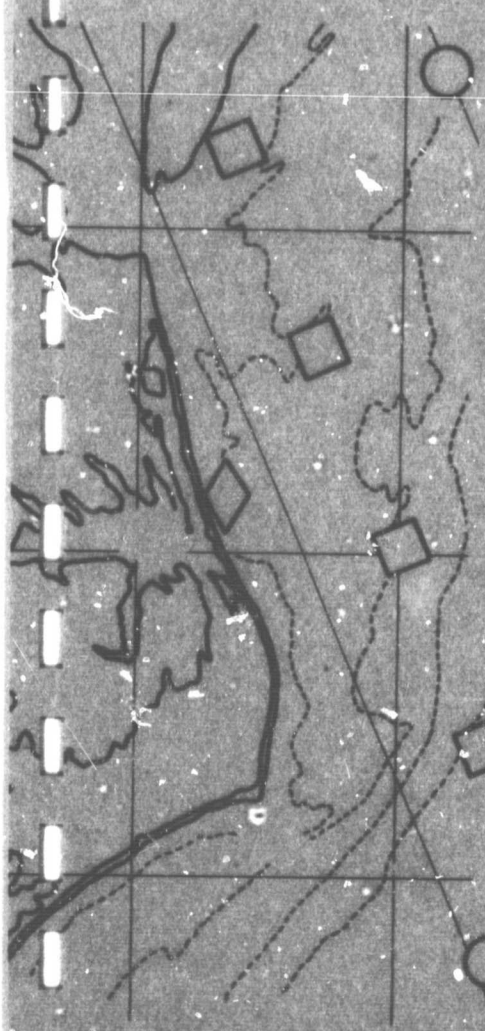

THE SEASAT SAR WIND AND OCEAN WAVE MONITORING CAPABILITIES

A CASE STUDY FOR PASS 1339M, 28 SEPTEMBER, 1978

ROBERT C. BEAL

THE JOHNS HOPKINS UNIVERSITY ■ APPLIED PHYSICS LABORATORY
Johns Hopkins Road, Laurel, Maryland 20810

PB80-194996

The Seasat SAR Wind and Ocean Wave Monitoring Capabilities, A Case Study for Pass 1339M 28 September, 1978

Johns Hopkins Univ.
Laurel, MD

Prepared for

National Oceanic and Atmospheric Administration
Rockville, MD

Jan 80

U.S. Department of Commerce
National Technical Information Service
NTIS

NOAA FORM 25-13 (1-78)

BIBLIOGRAPHIC DATA SHEET

U. S. DEPARTMENT OF COMMERCE
NATIONAL OCEANIC AND ATMOSPHERIC ADMINISTRATION

1. NOAA ACCESSION NUMBER	2.	3. RECIPIENT'S ACCESSION NUMBER
NOAA-80050104		PB80 194996

4. TITLE AND SUBTITLE
The Seasat SAR Wind and Ocean Wave Monitoring Capabilities
A Case Study for Pass 1339M, 28 September, 1978

5. REPORT DATE
Aug 1979 (Rev. 1980)

6.

7. AUTHOR(S)
Robert C. Beal

8. REPORT NO.
JHU/APL SIR 79U-019

9. PERFORMING ORGANIZATION NAME AND ADDRESS
The Johns Hopkins University,
Laurel, MD 20810,
Applied Physics Laboratory

10. PROJECT/TASK NO.

11. CONTRACT/GRANT NO.
MO-A01-78-00-4330

12. SPONSORING ORGANIZATION NAME AND ADDRESS
National Oceanic and Atmospheric Administration; and
National Aeronautics Space Administration,
Seasat Announcement of Opportunity Program

13. TYPE OF REPORT AND PERIOD COVERED

14.

15. PUBLICATION REFERENCE
The Johns Hopkins University, Applied Physics Laboratory Report No. JHU/APL SIR 79U-019, August 1979, Revided January 1980. 63 p, 22 fig, 1 tab, 19 ref, photo, append.

16. ABSTRACT
One of the primary purposes of the Seasat Synthetic Aperture Radar (SAR) was to explore the possibility for synoptic monitoring of ocean wavelength and direction from space. "Duck-X" (acronym for Duck, North Carolina Experiment) was one of only three or four major Seasat SAR wave detection experiments conducted with extensive coincident surface truth during the limited lifetime of the SAR. On the 28th of Sept., a well organized low energy 11 sec. swell system off the East Coast of the U.S. was detected with the Seasat SAR and successfully tracked from deep water, across the continental shelf, and into shallow water. In addition, a less organized 7 sec. system has been tentatively identified in the imagery. Both systems were independently confirmed with simultaneous wave spectral measurements from a research pier, aircraft laser profilometer data, and Fleet Numerical Spectral Ocean Wave Models. (A note added in revision) Recent comparative analysis performed by APL of the SAR system impulse response function of several SAR processing systems indicates that a double response sometimes occurs in the JPL optical processor. The separation between doublets is approx. 50 to 80 m, and is nearly in the range dimension. This appears to be a potential mechanism for "creating" waves in the range dimension where none actually exist. Therefore the results reported here and elsewhere for wavelengths of 100 m or less should be interpreted cautiously. (Author modified)

17. KEY WORDS AND DOCUMENT ANALYSIS

17A. DESCRIPTORS

*Monitoring, *Wave detection, *Wavelengths, *Ocean waves, Remote sensing, Wind (Meteoroloty), Wind velocity

17B. IDENTIFIERS/OPEN-ENDED TERMS

Satellite data, Seasat, Synthetic Aperture Radar (SAR)

17C. COSATI FIELD/GROUP

8J, 4B

18. AVAILABILITY STATEMENT
Released for distribution:
Elaine L. Downs

19. SECURITY CLASS (This report)	21. NO. OF PAGES
UNCLASSIFIED	
20. SECURITY CLASS (This report)	**22. PRICE**
UNCLASSIFIED	

NOAA FORM 25-13 (1-78) SUPERSEDES ALL PREVIOUS EDITIONS.

JHU/APL
SIR 79U–019
AUGUST 1979
REVISED
JANUARY 1980

THE SEASAT SAR WIND AND OCEAN WAVE MONITORING CAPABILITIES

A CASE STUDY FOR PASS 1339M, 28 SEPTEMBER, 1978

ROBERT C. BEAL

THE JOHNS HOPKINS UNIVERSITY ■ APPLIED PHYSICS LABORATORY
Johns Hopkins Road, Laurel, Maryland 20810

THE JOHNS HOPKINS UNIVERSITY
APPLIED PHYSICS LABORATORY
LAUREL, MARYLAND

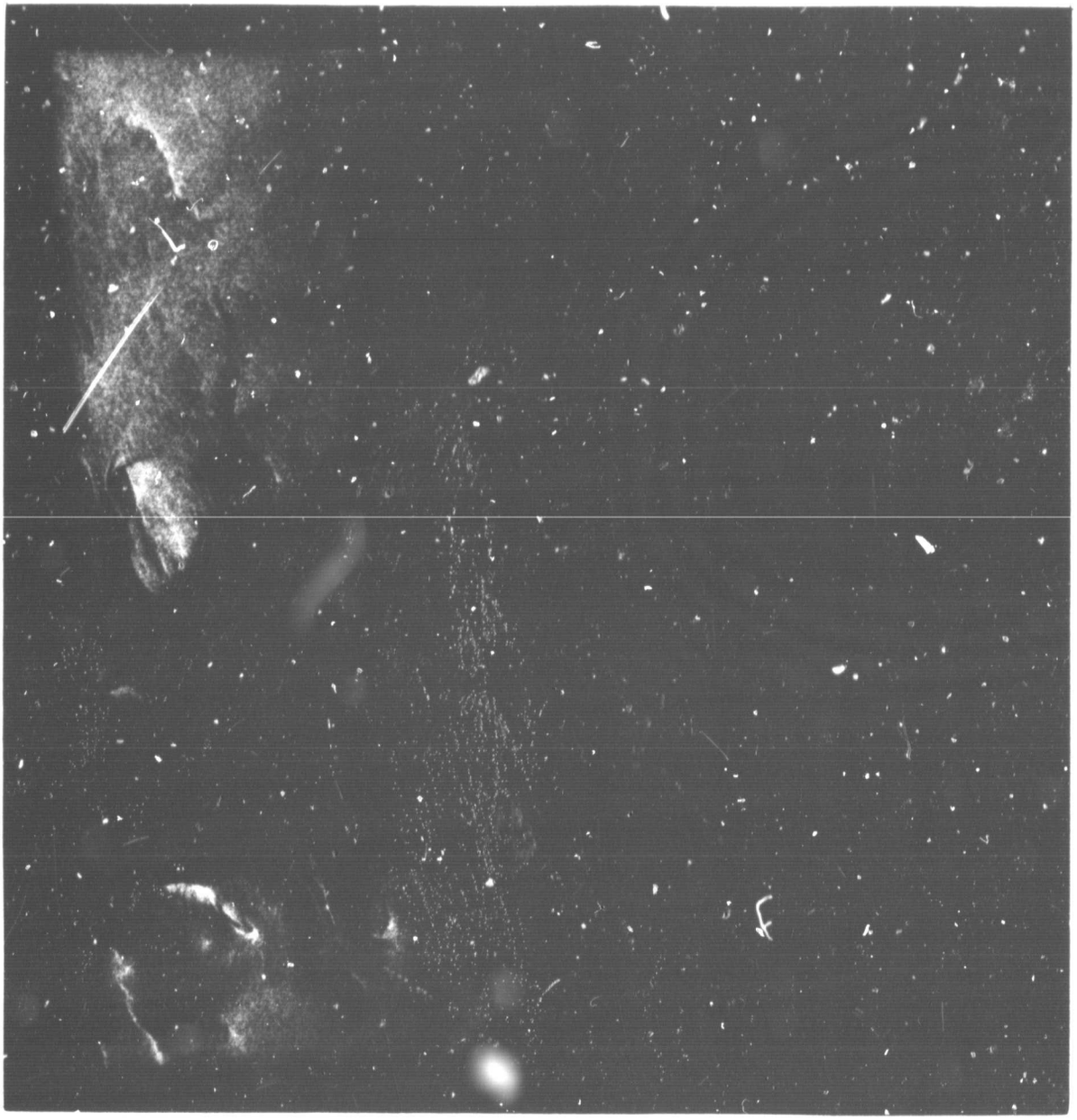

Complex radar backscatter patterns in a nearly calm region of the ocean located just outside the mouth of the Chesapeake Bay, captured by the SEASAT imaging radar, 28 September 1978. The dark regions generally correspond to low surface winds (less than 2 m/s), but the patterns also indicate a wide variety of surface interactions having little relationship to the wind.

THE JOHNS HOPKINS UNIVERSITY
APPLIED PHYSICS LABORATORY
LAUREL MARYLAND

TABLE OF CONTENTS

Foreward

This report, although final in the contractural sense, is only interim in the scientific sense. The major conclusion, that the Seasat SAR accurately measured ocean wavelength and direction, both in deep water and near-shore, under the conditions described in this report, is unlikely to be revised. Subtleties of the measurement technique, however, require further work, both intensively on the particular pass examined here, and extensively, using the entire data bank legacy from Seasat. In particular, work remains to be done on the bounds of SAR ocean wave detection, and the behavior of the radar scattering mechanism which governs this detection.

The work described in this report was jointly supported by the National Oceanic and Atmospheric Administration and the National Aeronautics and Space Administration as a portion of the Seasat Announcement of Opportunity Program under Contract Number MO-A01-78-00-4330.

Acknowledgements

The timely analysis of satellite data is never possible without the cooperation of many people. It is a pleasure to specifically acknowledge the help of the following individuals: W. Brown of the Jet Propulsion Laboratory for providing extensive reprocessing of SAR Pass 1339, and the accompanying optical transforms; D. Lichy of the U.S. Army Corps of Engineers, Coastal Engineering Research Center, for the wave gage data of Figure 12 and for the overall logistics coordination of the Duck-X supplementary data collection; D. Ross of the National Oceanic and Atmospheric Administration/Sea-Air Interaction Laboratory for the aircraft laser profilometer and side-looking airborne radar data of Figures 11 and 14; E. M. Bracelante of National Aeronautics and Space Administration/Langley Research Center for the Seasat scatterometer wind vector analysis which formed the basis of Figure 18; E. Walsh of National Aeronautics and Space Administration/Wallops Flight Center for the altimeter data of Figure 21; F. Gonzalez of National Oceanic and Atmospheric Administration/Pacific Marine Environmental Laboratory for obtaining the FNWC products as a portion of the GOASEX II data request, and J. Jenkins of the Applied Physics Laboratory/The Johns Hopkins University for optimizing the image enhancement algorithms of Figure 15. Figure A-4 is composed of information supplied by the Jet Propulsion Laboratory Mission Analysis Office.

P. DeLeonibus and J. Ernst of National Oceanic and Atmospheric Administration/National Environmental Satellite Service and L. Harris of the U.S. Army Corps of Engineers, Coastal Engineering Research Center, provided helpful suggestions in the draft report stage.

THE JOHNS HOPKINS UNIVERSITY
APPLIED PHYSICS LABORATORY
LAUREL MARYLAND

THE SEASAT SAR
WIND AND OCEAN WAVE MONITORING CAPABILITIES
A Case Study for Pass 1339M
28 September 1978

ABSTRACT

One of the primary purposes of the Seasat Synthetic Aperture Radar (SAR) was to explore the possibility for synoptic monitoring of ocean wavelength and direction from space. "Duck-X" (an acronym for the Duck, North Carolina Experiment) was one of only three or four major Seasat SAR wave detection experiments conducted with extensive coincident surface truth during the limited lifetime of the SAR.

On the 28th of September, a well organized low energy (H_s < 1 m) 11 second swell system off the East Coast of the U. S. was detected with the Seasat SAR and successfully tracked from deep water, across the continental shelf, and into shallow water. In addition, a less organized 7 second system has been tentatively identified in the imagery. Both systems were independently confirmed with simultaneous wave spectral measurements from a research pier, aircraft laser profilometer data, and Fleet Numerical Spectral Ocean Wave Models.

A comparison of the SAR radar backscatter power with the Seasat Scatterometer System (SASS) inferred wind speed indicates a power law dependence of SAR backscattered power, $\sigma_o \sim U^{0.65}$ over a surface wind speed range of 4 m/s $\leq U_{10} \leq$ 14 m/s.

Note added in revision: Recent comparative analysis performed by APL of the SAR system impulse response function of several SAR processing systems indicates that a double response sometimes occurs in the JPL optical processor. The separation between doublets is approximately 50 to 80 meters, and is nearly in the range dimension. This appears to be a potential mechanism for "creating" waves in the range dimension where none actually exist. Therefore the results reported here (pp 26 and 27) and elsewhere for wavelengths of 100 m or less should be interpreted cautiously.

THE JOHNS HOPKINS UNIVERSITY
APPLIED PHYSICS LABORATORY
LAUREL MARYLAND

THE SEASAT SAR
WIND AND OCEAN WAVE MONITORING CAPABILITIES
A Case Study for Pass 1339M
28 September 1978

1.0 SUMMARY

A number of aircraft studies in the past few years have indicated that ocean swell can be reliably imaged with Synthetic Aperture Radar (SAR) at least for some values of wind velocity when there is a substantial component of the swell travelling along the line-of-sight of the radar (Brown et al., 1976; Elachi, 1976; Elachi et al., 1977; Shuchman et al., 1978; Teleki et al., 1978). The bounds of wind, wave and geometric conditions over which reliable ocean wave detection occurs, however, remain elusive for want of an extensive experimental data base. Seasat provided a unique, although limited, opportunity to re-examine the wave detection problem without some of the artificial constraints of aircraft measurements. Jordan (1978) gives a concise summary of the Seasat SAR design parameters. A general description of the total Seasat SAR system and a prediction of some of its fundamental information limitations is given by Beal et al. (1977) and Beal (1978). A preliminary assessment of the Seasat SAR ocean wave detection capabilities is given by Gonzalez et al. (1979).

During the limited 100 day lifetime of the Seasat SAR, nearly 500 passes of duration ranging from 1 to 15 minutes were collected at three domestic and two foreign receiving stations. Twenty-three of these passes provided acceptable SAR imagery within 70 km of a well instrumented research pier operated by the U.S. Army Corps of Engineers, Coastal Engineering Research Center (CERC) at Duck, North Carolina. The CERC facility at Duck has been described by Mason (1979). Table I summarizes the total data set collected at the Duck site during the Seasat lifetime. The Applied Physics Laboratory of The Johns Hopkins University (APL), along with several government agencies, collected a variety of wind and wave measurements during a concentrated eight week period from August 12 to October 9, 1978.

THE JOHNS HOPKINS UNIVERSITY
APPLIED PHYSICS LABORATORY
LAUREL, MARYLAND

Table 1

Data summary of the SEASAT SAR wave detection experiment, 1978, Duck, N.C.

APL RUN NO.	LOCAL DATE	LATITUDE ON	LATITUDE OFF	OVERPASS TIME (GMT)	ID NO.	REV NO.	SURFACE TRUTH	A/C SLAR	SHORT WAVE SPECTRUM	SIGNIFICANT WAVEHEIGHT (m) (20 min av)	PREDOMINANT PERIOD (5 min av)	WIND VELOCITY (m/s)	COMMENTS
	9 Jul	14	46	09:35:29	006	0177	I		---				Probable direct overpass,poor tape
	23 Jul	13	70	10:41:50	051	0378	I		---				~10 km to the West
	24 Jul	8	43	00:05:08	058	0400	I		Night				Probable direct overpass
	27 Jul	8	43	00:12:12	069	0443	W/W		Night				~100 km to the East,poor tape
	13 Aug	8	43	09:25:33	147	0687	W/W	X	Night				~70 km to the East
	24 Aug	22	37	02:18:15	197	0845	W/W	X	Night				Probable direct overpass
	27 Aug	32	51	02:28:33	210	0888	I		Night				~30 km to the East
02	29 Aug	30	37	13:14:50	216	0909	W/W/L	X	Good		8	SSW6	Direct overpass
	30 Aug	32	49	02:40:52	226	0931	I		Night				~40 km to the East
	1 Sep	30	37	09:27:09	230	0952	W/W		---				Direct overpass;Hurricane Ella;no SAR tape
	2 Sep	33	49	02:53:11	240	0974	W/W	X	Night				~50 km to the East
03	4 Sep	30	37	13:39:28	245	0995	W/W/L	X	Good	0.64	10	NNW6	Possible direct overpass(≤10 km),poor tape
04	7 Sep	32	35	13:51:47	261	1038	W/W/L		Fair		10	WSW1	Possible direct overpass(≤10 km)
06	10 Sep	33	36.5	14:04:05	271	1081	W/W/L		Poor				Possible direct overpass(≤10 km)
07	13 Sep	21	31	14:17:07	284	1124	W/W	X	Good				SAR turned off 5° early;no SAR tape
08	16 Sep	13	30	14:29:41	295	1167	W/W		Good	0.84	8		SAR turned off 4° early
10	19 Sep	27	37	14:42:26	314	1210	W/W		Fair	0.40	7	SSW5	Possible direct overpass(≤10 km)
	21 Sep	22	55	04:08:42	327	1232	I		Night				~70 km to the East
18	22 Sep	15	42	14:55:12	339	1253	W/W		Good	0.57	7	SW4	15 km to the East
	24 Sep	35	45	00:21:28	353	1275	I		Night				~70 km to the East;Shoe Cove only
19	25 Sep	28	41	15:08:03	365	1296	W/W	K	Fair	0.8	7	N4	15 km to the East
	27 Sep	36	49	00:34:20	379	1318	I		Night				~70 km to the East;Shoe Cove only
21	28 Sep	27	41	15:20:50	388	1339	W/W/L	K,X	Good	1.0	11/7*	N2	20 km to the East
	30 Sep	36	50	00:47:07	402	1361	I		Night				~70 km to the East;no SAR tape
22	1 Oct	27	40	16:33:38	411	1382	W/W/L		Poor	1.28	8		Possible direct overpass
	3 Oct	6	56	04:59:47	425	1404	I		Night				~70 km to the East
23	4 Oct	18	38	15:46:16	435	1425	W/W/L		Poor	0.84	7*		Possible direct overpass(≤10 km)
	6 Oct	6	55	05:12:30	448	1447	I		Night				~70 km to the East
24	7 Oct	21	41	15:58:59	458	1468	W/W/L		Fair	1.36	14*	NNW6	Direct overpass
	9 Oct	6	65	05:25:15	471	1490	I		Night				~70 km to the East

LEGEND

I: surface truth must be inferred
W/W: wind and long wave records are available
W/W/L: surface L-band radar also available
X: LaRC X-band A/C SLAR present
K: NOAA/SAIL K-band A/C SLAR present
*: 20 minute average

Of all the passes collected during the eight week period of intensive sea truth measurements, one particular four-minute pass has associated with it a peculiar combination of properties which, although not yielding a complete set of conditions, nevertheless warrants special attention. Therefore, although a large volume of oceanographic data is available for eventual analysis as a result of Seasat, this paper deals with one pass exclusively.

On the morning of September 28, 1978, at 1520 GMT, Seasat approached the east coast of the United States, with the SAR (100 km) swath running approximately parallel to the coast, but displaced eastward by about 20 km. On the basis of the present analysis of that pass, several major conclusions are listed:

(1) the SAR can successfully detect low energy swell systems of significant wave height, H_s, well under 1 m (actually 0.65 m $\pm$ 0.25 m).

(2) diffraction of low energy but well organized swell due to local ocean depth changes is clearly detectable in both wavelength and direction.

(3) the complexity of the ocean spectrum (e.g., whether it is composed of more than one system, or is spread in direction and wave number) seems to have little bearing on the threshold detection limits.

(4) the average backscatter at the SAR interaction wavelength of 30 cm is directly related to the surface wind speed as measured by the Seasat scatterometer (SASS), that is, as inferred through an algorithm from SASS backscatter measurements at 3 cm.

The above four statements represent a strong positive endorsement for an instrument that drew widely varying opinions with respect to its oceanographic utility prior to launch. The statements should be balanced, however, with the following caveats,

which this paper does not address due to the lack of sufficient data:

(1) the ability of the SAR to detect long wave systems has been confirmed only for the range of surface winds from 4-14 m/s.

(2) geometric independence of the SAR wave detectability with respect to direction of wave travel has not been confirmed unequivocably.

(3) no reliable algorithm for yielding an ocean wave energy spectrum from the image spectrum has been developed in this effort.

To address these areas and the more general question of the utility of SAR in space, further examination of the large body of existing Seasat data will be necessary. The several on-going or planned workshops (GOASEX, STORMS, DUCK-X, and JASIN) are helping to expand our data set, and the ability to make broader generalizations regarding the utility of Seasat, and in particular the SAR.

2.0 AUXILIARY DATA SOURCES FOR 28 SEPTEMBER

2.1 National Weather Service

The National Weather Service (NWS) Surface Analysis for 1500 GMT 28 September (Figure 1) illustrates the general conditions in the region of interest twenty minutes prior to the time of overpass. A loosely organized low pressure system was developing and strengthening off the New England coast. A low pressure trough extended from the Gulf of Maine southward past 30°N latitude. The entire system formed the primary source of wind and short period (i.e., 6 to 10 sec) waves which were measured by Seasat. According to ship or station reports shown in Figure 1, surface winds peaked at between 9 and 11 m/s (~20 Kts) in a region around 35°N to the west of the trough, and were generally northerly. Further to the north (39°N,70°W) the winds continued to be moderately strong (7.5 m/s or 15 kts), following the trough boundary. To the east

THE JOHNS HOPKINS UNIVERSITY
APPLIED PHYSICS LABORATORY
LAUREL, MARYLAND

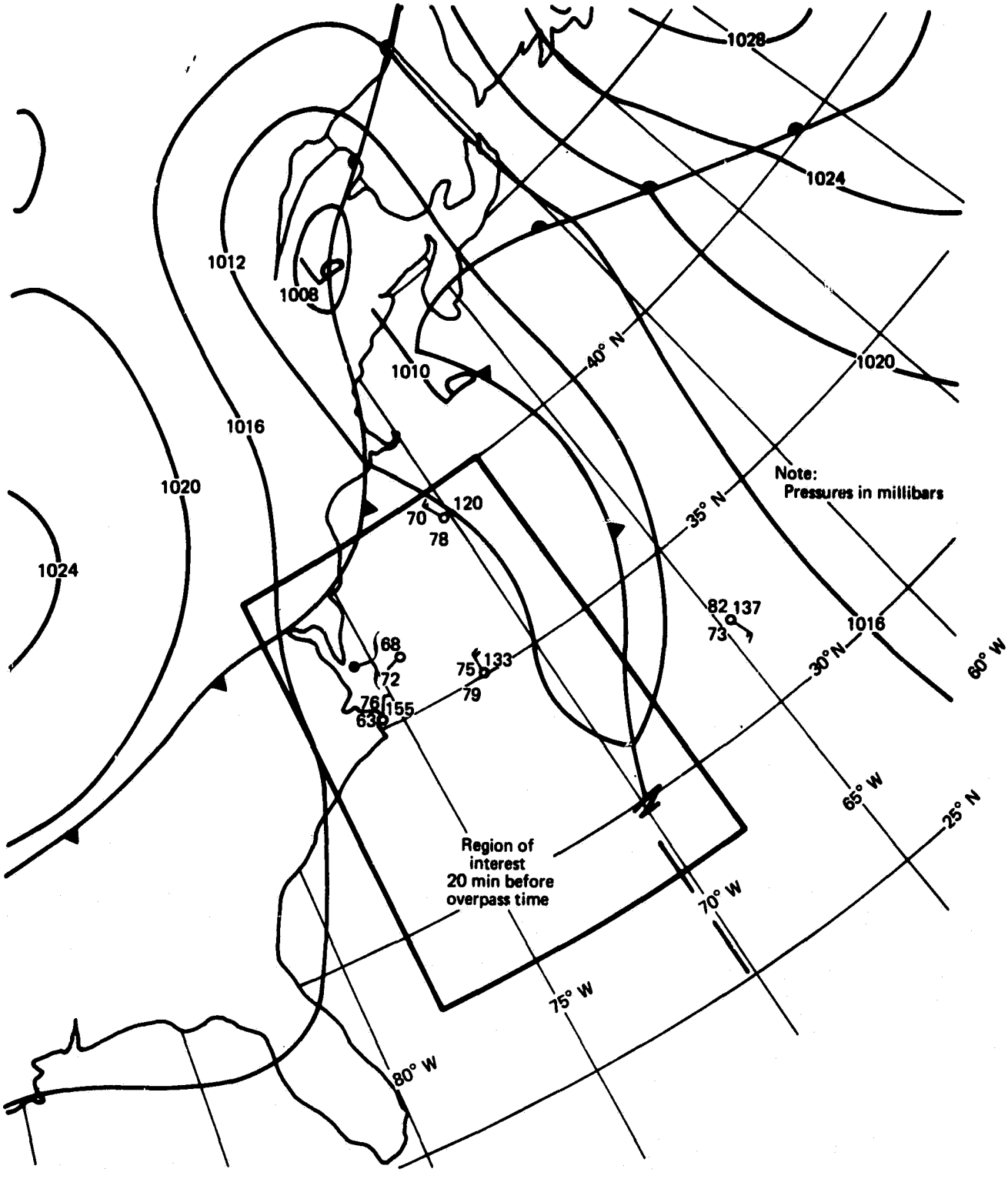

Fig. 1 National Weather Service off-shore surface analysis for 1500 GMT, 28 Sept, 1978.

of the trough (32°N, 65°W) southerly winds indicate a counter-clockwise flow of air around its southern edge. A station report close to the mouth of the Chesapeake, and just below an approaching cold front, indicates a near-calm (1 to 2 kts, or < 1 m/s). Based on the information in Figure 1 then, a fairly wide range of wind conditions existed within the region of interest around the time of overpass, which produced a correspondingly wide range of wave conditions.

For reference, the Geostationary Operational Environmental Satellite (GOES) visible and infrared photos are shown in Figures 2 and 3, respectively. Figure 2 shows the prevailing cloud cover, and perhaps suggests a general wind circulation pattern. The infrared photo of Figure 3 displays a combination of cloud and ocean temperature. The two pronounced cold regions to the right (corresponding to dark on the photo) are associated with, but not coincident with, the low pressure trough of Figure 1. The radar summary of Figure 4 indicates only a small region of precipitation just to the south of Cape Hatteras moving due East. The major portion of the region of interest, however, appears to be free of precipitation.

2.2 Fleet Numerical Weather Central

The Navy Fleet Numerical Weather Central (FNWC) Spectral Ocean Wave Model (SOWM) (Lazanoff and Stevenson, 1975) further corroborates and expands the knowledge of the wind and wave conditions at overpass time. Figure 5 summarizes the FNWC estimates of significant wave height, H_s, contours three hours before overpass time. There are two localized regions of $H_s > 1.9$ m (>6 ft). In general, however, the figure indicates that an estimate of $1 \text{ m} \leq H_s \leq 2 \text{ m}$ applies to essentially the entire region of interest at overpass time.

FNWC derives the significant wave height estimates from a surface wind model based on available ship and station reports. These reports are merged into a global matrix of wind and wave conditions referred to a standard grid system. SOWM grid point

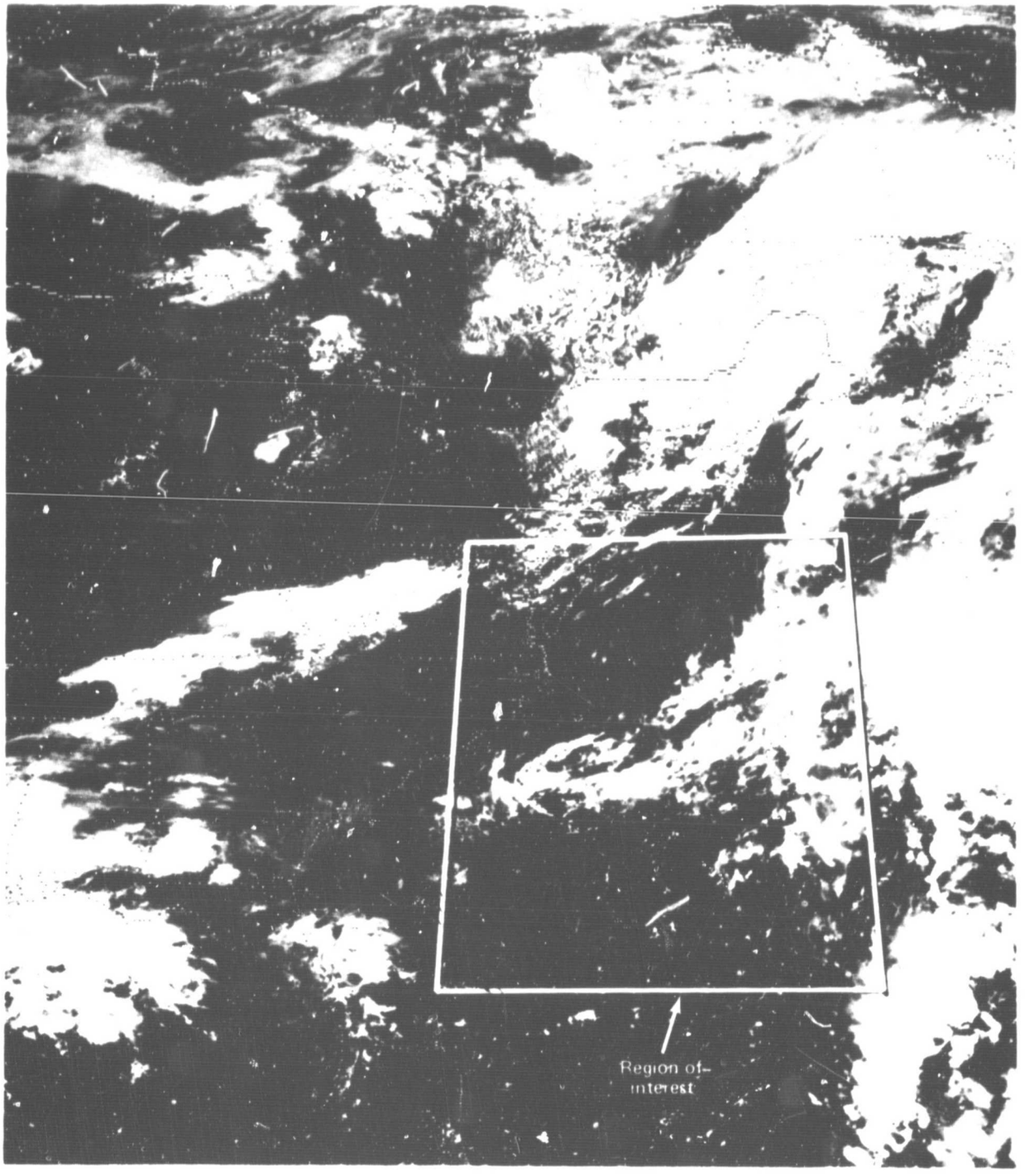

Fig. 2 GOES visible imagery 10 minutes after SEASAT overpass, 1530 GMT, 28 Sept, 1978.

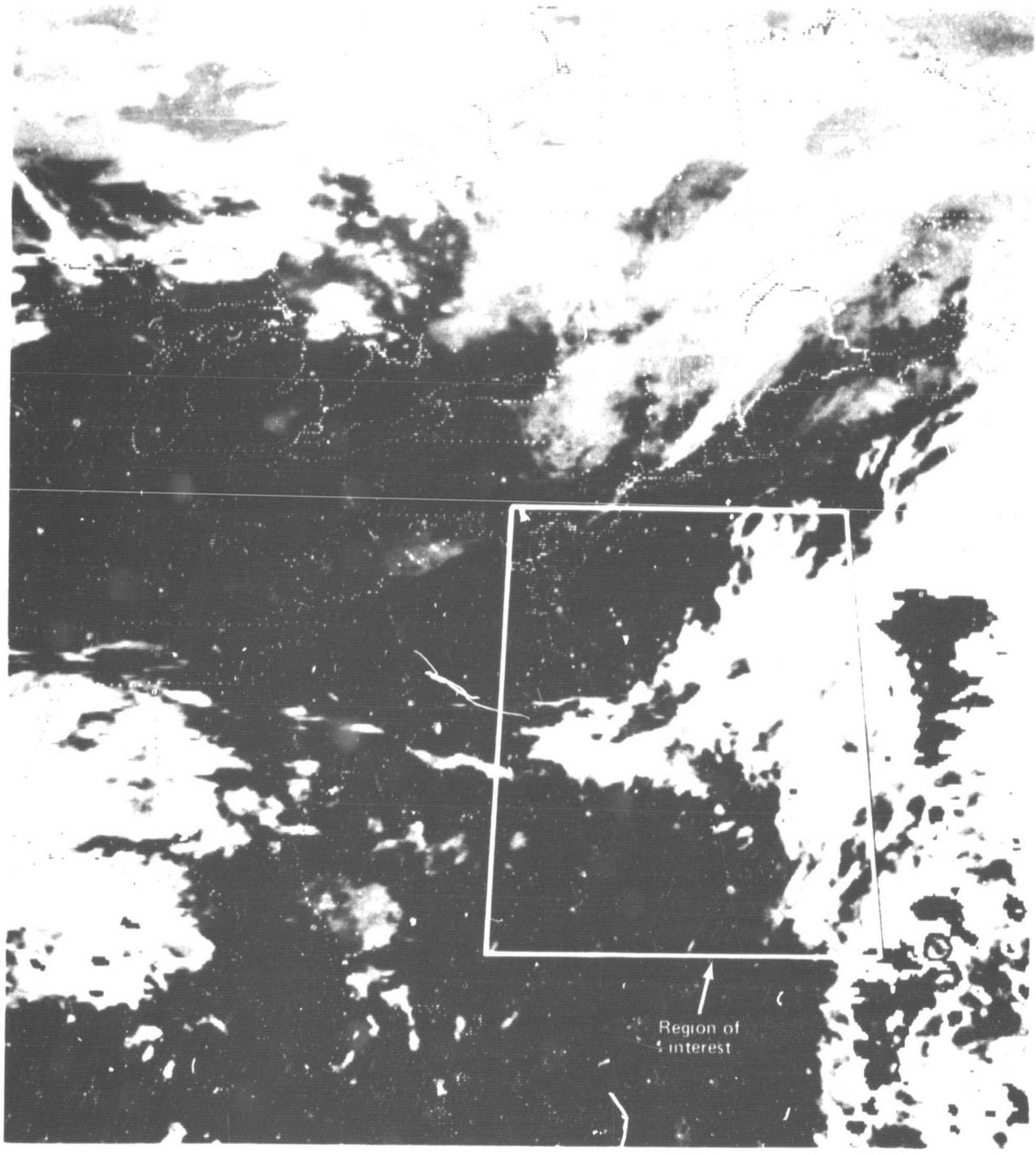

Fig. 3 GOES IR imagery 20 minutes before SEASAT overpass, 1500 GMT, 28 Sept, 1978.

THE JOHNS HOPKINS UNIVERSITY
APPLIED PHYSICS LABORATORY
LAUREL, MARYLAND

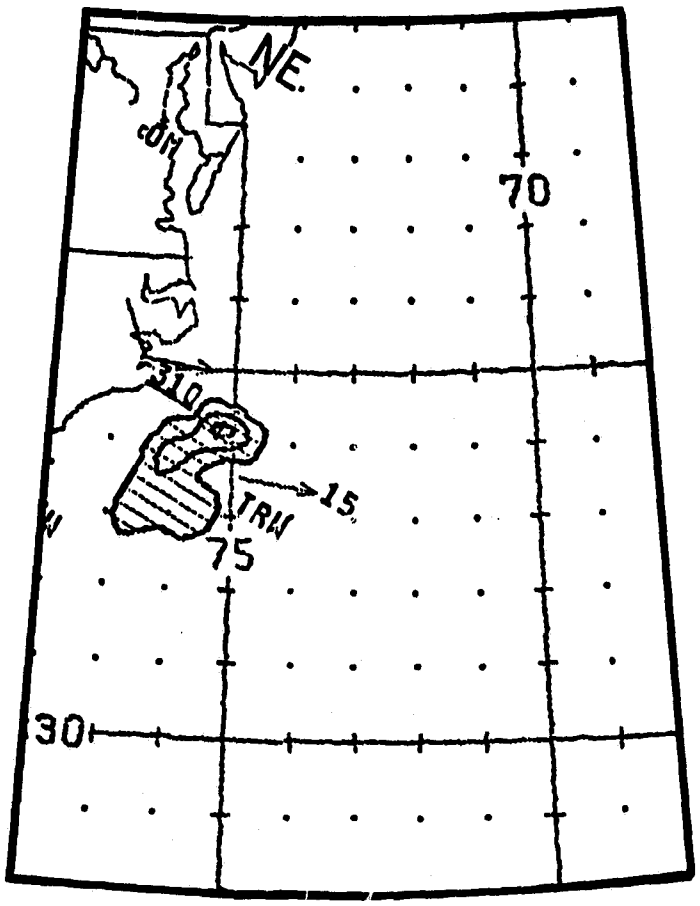

Fig. 4 National Weather Service Radar Summary Chart in area of interest 15 minutes after overpass, 1535 GMT, 28 Sept, 1978.

THE JOHNS HOPKINS UNIVERSITY
APPLIED PHYSICS LABORATORY
LAUREL, MARYLAND

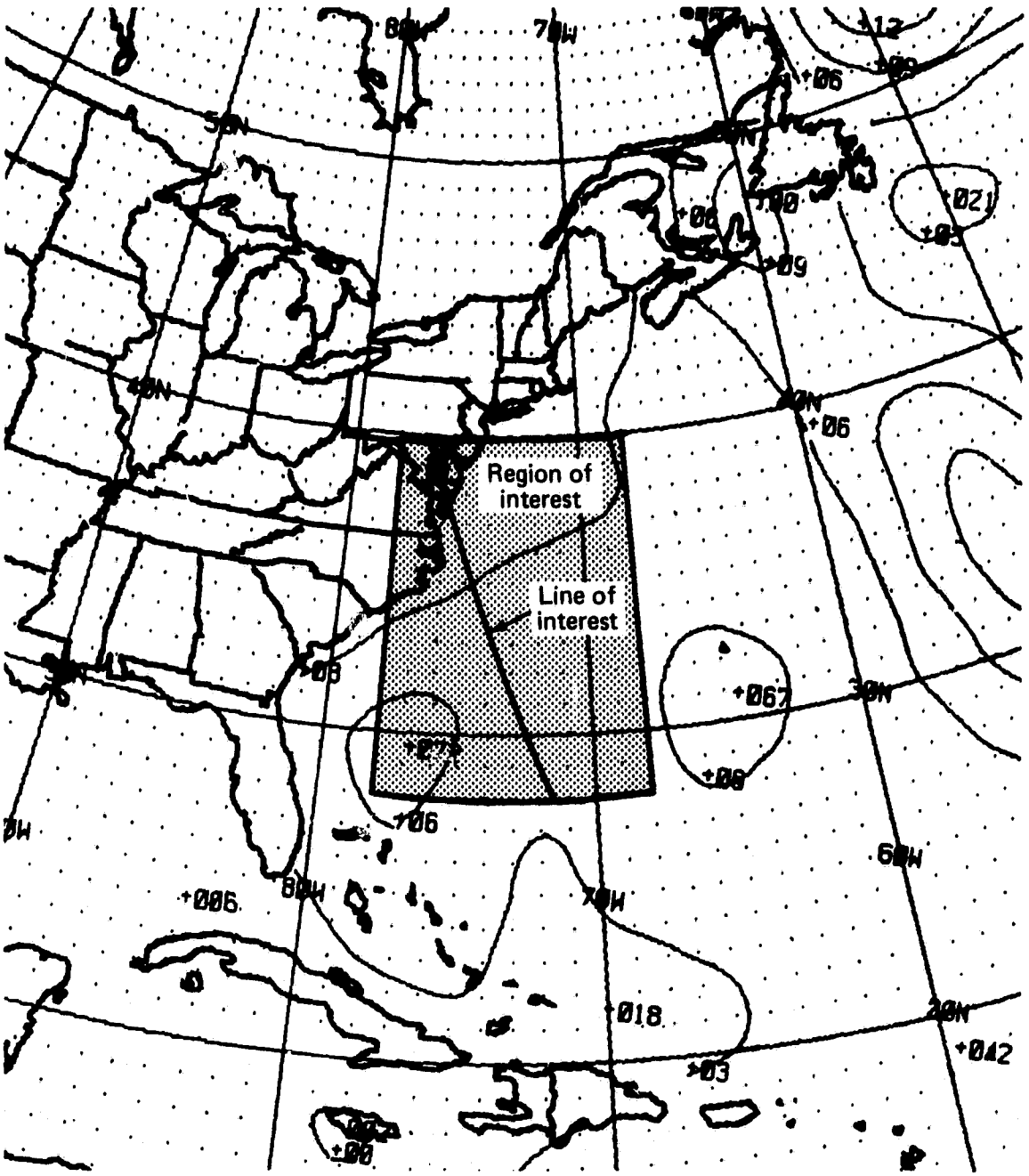

Fig. 5 Fleet Numerical Weather Central significant wave height surface analysis $3^h\ 20^m$ prior to overpass time, 1200 GMT, 28 Sept, 1978. Notations are in feet.

locations in the area of interest are shown in Figure 6. Figure 7 shows the evolving directional wave energy spectrum referenced to the grid system of Figure 6. The plots of energy density versus reciprocal wavelength and direction clearly indicate two wave systems of varying degrees of organization along the path of interest. The long wave system has an average wavelength of about 200 meters (11 second period), and is reasonably constant in energy over a 5^{o} change in latitude. This is an ESE swell generated by a remote source of several days earlier, and several hundred kilometers removed from the region of interest. The shorter 75 m (7 second) system, however, shows a rapid evolution in the same 5^{o}, because it is more closely coupled with the accompanying wind field. The southern-most SOWM plots, being widely dispersed in angle, reflect a recently changing wind field, while the most northerly grid points reflect a relatively more stable wind field.

Table II is a summary of FNWC wind and wave height for the twelve hour period around overpass time in the region of interest. Additionally, the table shows the frictional wind velocity estimates, and separate estimates of long and short wave "equivalent" significant wave height. Using directional wave energy spectral plots, the total energy is divided into two components above and below 0.1 Hz (10 sec period). The division is chosen based on an examination of the spectra in Figure 7, and is an attempt to bifurcate the composite system into one longer, less wind dependent, and a second shorter, more wind dependent, system. Figure 8 shows graphically the results of such a division based on the 1500 GMT portion of Table II.

The wind magnitude and short (5-10 sec) wave energy track well through the region of interest, both simultaneously experiencing local peaks, while the underlying 11 second swell system is relatively invariant in energy. It should be noted that the FNWC total energy estimates of both systems combined corresponds to a significant wave height of under 1 meter above 34^{o}N. Separate aircraft and surface measurements to be described in the next section will further refine this energy estimate.

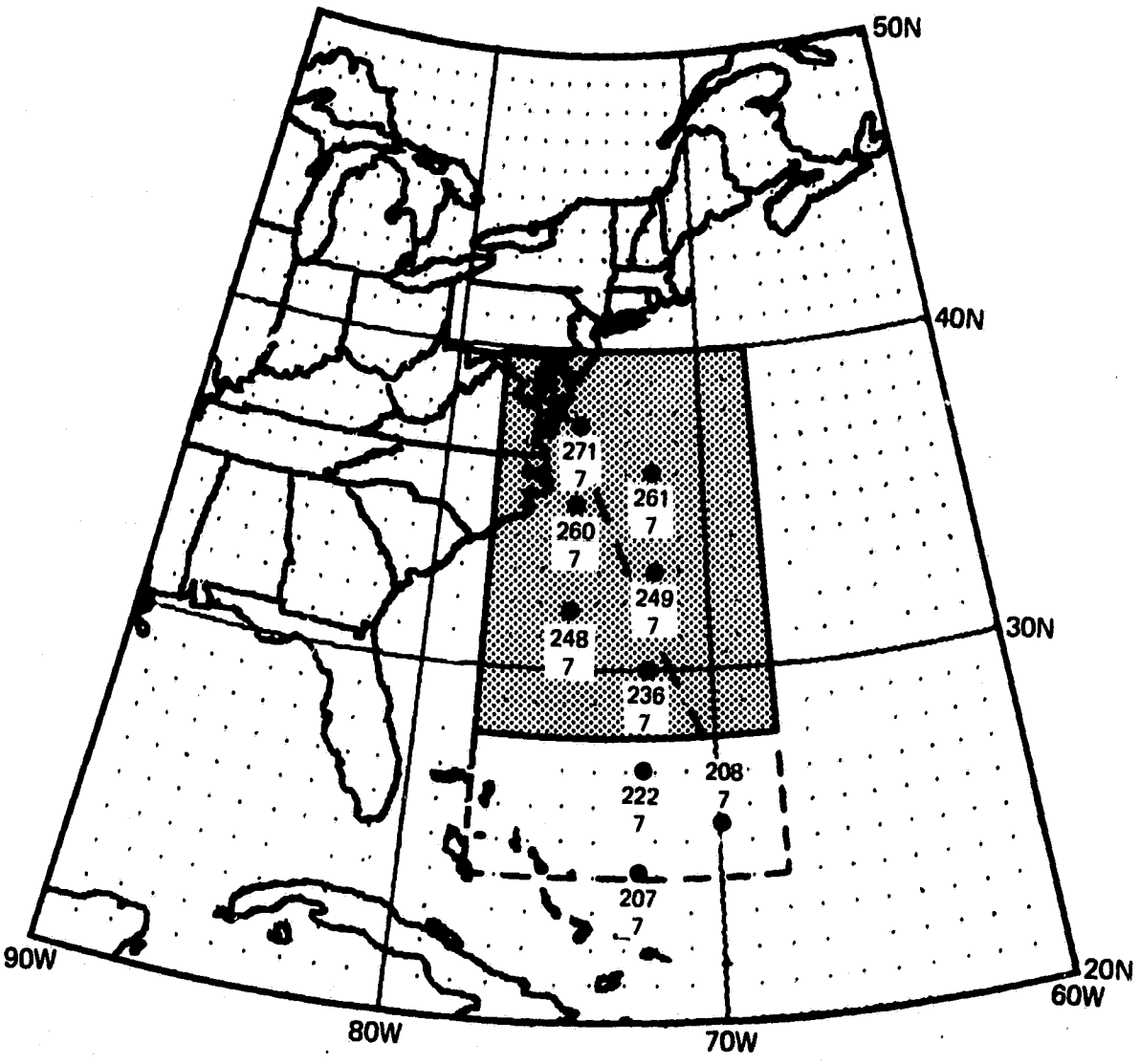

Fig. 6 Fleet Numerical Weather Central reference grid index.

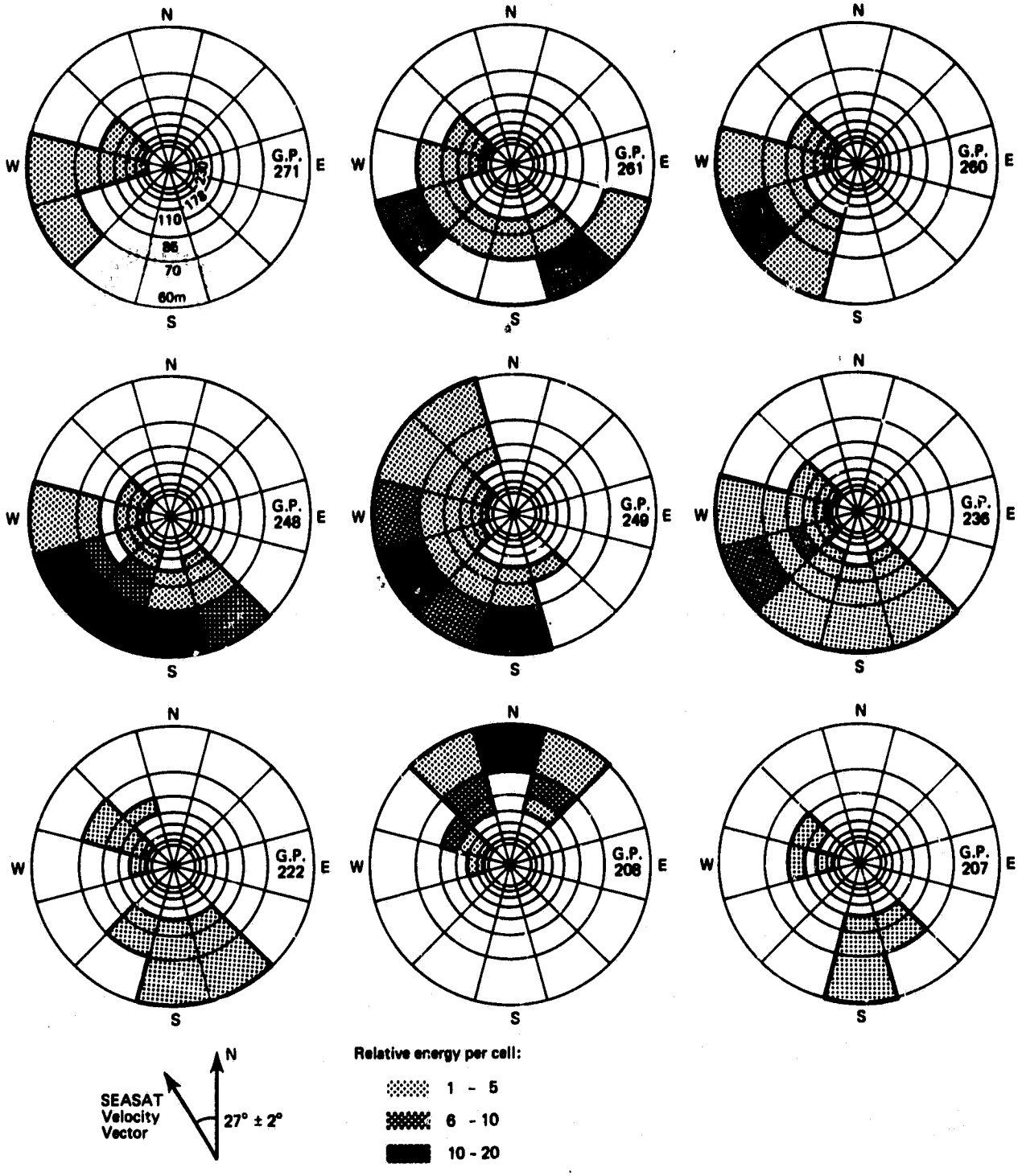

Fig. 7 Selected Fleet Numerical Weather Central surface ocean wave two dimensional energy spectra for 1500 GMT, 28 Sept, 1978 in the region of interest. Radial distance from the center is proportional to reciprocal wavelength (wave number). For example, at grid point 207, a longer wave train is travelling from the ESE, and a shorter one from the NNW.

Table II

A temporal and spatial history of the FNWC SOWM within 6 hours of overpass time in the region of interest.

FNW GRID POINT	0900 GMT					1500 GMT					2100 GMT				
	Wind	U*	$H_{s\ tot}$	H_{s1}	H_{s2}	Wind	U*	$H_{s\ tot}$	H_{s1}	H_{s2}	Wind	U*	$H_{s\ tot}$	H_{s1}	H_{s2}
271	↘ 2.3	.09	1.70	1.14	1.26	↘ 2.8	.10	1.70	0.98	1.39	↘ 4.0	.15	1.44	0.70	1.26
261	↙ 9.0	.29	3.49	3.10	1.60	↙13.3	.46	4.88	4.63	1.55	↓14.6$^{\Delta}$	.52	4.58	4.38	1.33
260	↓ 7.8	.28	3.02	2.80	1.13	↓ 8.7	.32	2.56	2.33	1.06	↙ 7.2	.25	2.08	1.79	1.06
249	↙12.1	.39	4.53	4.31	1.39	↙13.9$^{\Delta}$	.47	4.95	4.77	1.33	↙13.6$^{\Delta}$	.46	4.45	4.29	1.20
248	↙18.0$^{\Delta}$	.64	6.86	6.66	1.65	↙17.6$^{\Delta}$	.62	5.44	5.26	1.39	↓14.8$^{\Delta}$	.50	4.53	4.35	1.26
236	↙12.0	.39	4.35	4.12	1.39	↓ 9.3	.30	2.91	2.59	1.33	↘ 7.6	.24	2.83	2.56	1.20
222	↙ 5.0	.00	2.88	2.59	1.26	↘ 4.5	.18	2.37	2.20	0.89	↘ 6.1	.21	2.19	1.96	0.98
208	↙12.9	.42	4.85	4.73	1.06	↙10.4	.33	3.22	3.07	0.98	↗ 6.0	.20	1.96	1.79	0.80
207	↗ 8.7	.28	2.00	1.74	0.98	↗ 7.8	.26	1.79	1.60	0.80	↘ 5.0	.00	1.74	1.55	0.80

NOTE: The winds are given in nautical miles per hour, the frictional velocity, U* in nm/hr, and H_s is in feet. The total H_s is further separated into two component parts, H_{s1} and H_{s2}, representing energy above and below a 10 second period, which approximately defines the boundary between the two wave systems present on 28 September. Arrows indicate direction of wind, Δ indicates presence of whitecapping.

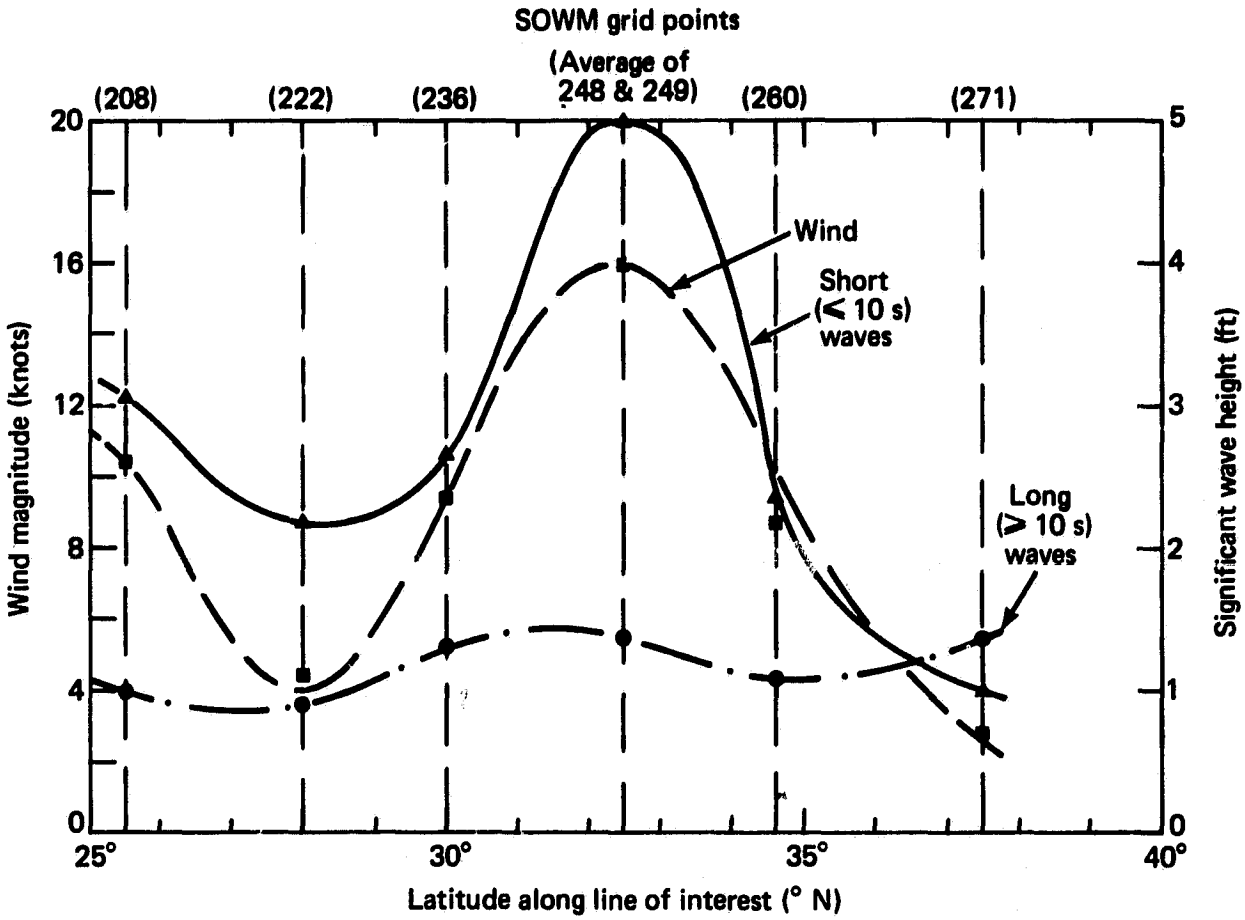

Fig. 8 FNWC derived estimates of the wind and waves referenced to line of interest at 1500 GMT, plotted from data in Table II.

3.0 SURFACE, AIRCRAFT, AND SPACECRAFT MEASUREMENTS

3.1 Types and Locations of Measurements for 28 September

Figure 9 shows the ground coverage of each of the three active instruments on Seasat (Altimeter, SASS, and SAR) as the spacecraft approached the U.S. East Coast. The SASS and SAR swaths passed just to the east of the CERC pier at Duck, N.C., while the altimeter subtrack passed several degrees to the west. The altimeter and SASS operated continually; the SAR, however, was enabled only to the north of 28°N, and this latitude forms the lower bound of the region of interest.

The highest concentration of surface and air measurements was located within 100 km of the CERC pier. Figure 10 identifies the various regions in the vicinity of Duck in which estimates or measurements of wind and waves were available. For reference, the edges of the 100 km SAR swath are shown by the solid lines inclined at approximately 27° with respect to north at this latitude. The locations are keyed in alphabetical order from north to south. Location A corresponds to FNWC grid point 271, the conditions at which have previously been presented in Figures 7 and 8 and Table II. Locations B, C, E, and F are 15 km square areas over which the SAR imagery has been optically Fourier transformed. Note that the local ocean depth (shown with dotted contours on Figure 10) changes appreciably over the 15 km square at locations B, C, and E. This would cause appreciable spreading of a single frequency deep water wave in both wavelength and direction. Deep water dispersion prevails only at location F for wavelengths greater than 70 m. Local depth changes at location B are especially severe, ranging from less than 10 m to at least 20 m. The National Oceanic and Atmospheric Administration (NOAA) aircraft laser profilometer spectra to be discussed in the next section were collected at location B. The Duck pier measurements, also to be discussed, were collected at location D. FNWC grid point 260 is represented by location G, and provides a convenient reference spectrum for the SAR imagery collected at location F. Locations F and G are the only "deep-water" locations of Figure 10.

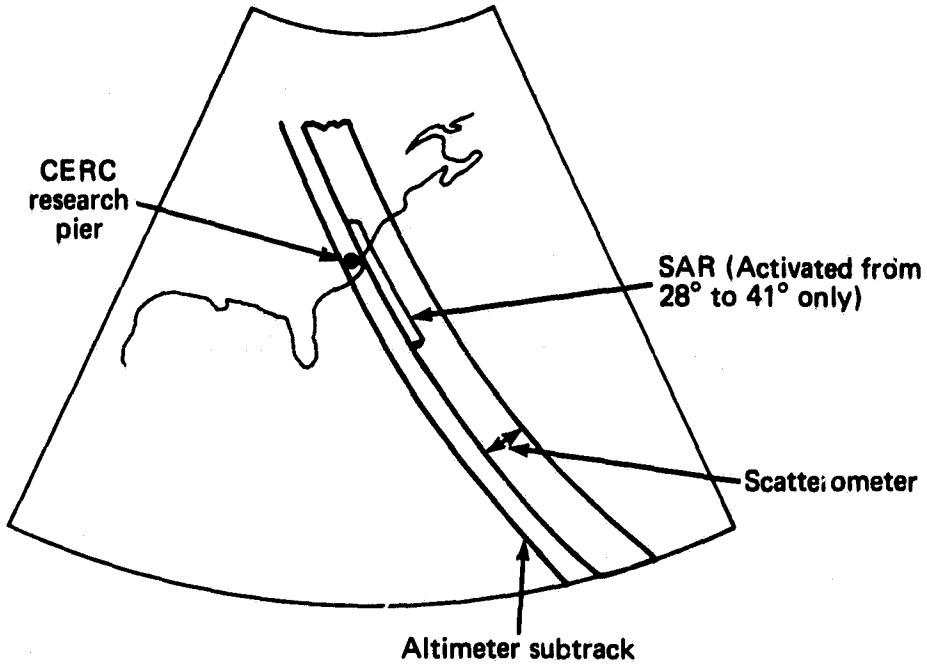

Fig. 9 SEASAT scatterometer (SASS), synthetic aperture radar (SAR) and altimeter coverage of the U. S. east coast region, 1510 GMT to 1525 GMT, 28 Sept, 1978.

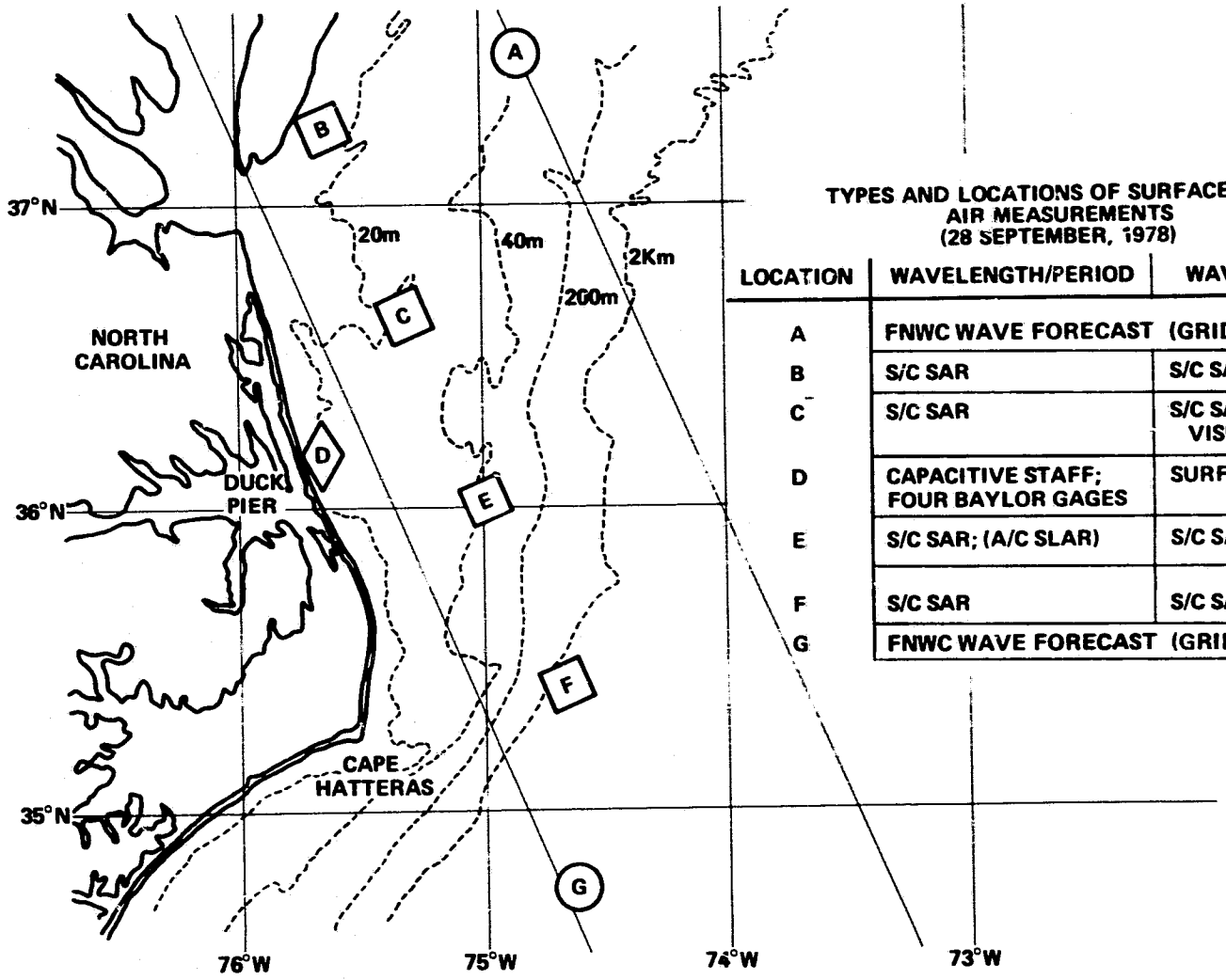

TYPES AND LOCATIONS OF SURFACE AND AIR MEASUREMENTS (28 SEPTEMBER, 1978)

LOCATION	WAVELENGTH/PERIOD	WAVE DIRECTION
A	FNWC WAVE FORECAST (GRID POINT 271)	
B	S/C SAR	S/C SAR
C	S/C SAR	S/C SAR; NOAA A/C VISUAL
D	CAPACITIVE STAFF; FOUR BAYLOR GAGES	SURFACE RADAR
E	S/C SAR; (A/C SLAR)	S/C SAR; A/C SLAR
F	S/C SAR	S/C SAR
G	FNWC WAVE FORECAST (GRID POINT 260)	

Fig. 10 Types and locations of surface and air measurements for 28 Sept, 1978 in the vicinity of Duck.

3.2 Surface Measurements of the One-Dimensional Long Gravity Wave Spectrum

Time histories of the long (>1 second) waves were recorded by five separate instruments in the vicinity of the CERC pier for a 20 minute interval spanning the overpass time. Figure 11 summarizes the one-dimensional long wave spectra measured in the vicinity of the CERC pier, from two Baylor gages, two wave rider buoys (Lichy, 1979), and one capacitive wave staff. The spectra show varying amounts of the 11 second and 7 second systems, but the average of the two gage and buoy measurements clearly identifies each system. The significant wave height derived from the averaged spectrum is 1.0 m, which of course, includes the combined energy from both the 11 second and 7 second systems. The significant wave height corresponding to each of the two systems (being roughly equal in energy at the pier) is closer to 0.7 m. By comparison, the FNWC SOWM grid point closest to the CERC pier (grid point #271, Table II, and Figure 8) yields a significant wave height of 0.4 m for the long wave system, and 0.3 m for the short wave system.

3.3 Aircraft Measurements of the One-Dimensional Long Gravity Wave Spectrum

A NOAA/Sea-Air Interaction Laboratory (SAIL) aircraft flying about 50 km to the east of Duck was equipped with a variety of instruments, including a laser profilometer (Ross and Cardone, 1970) capable of measuring the one-dimensional ocean height spectrum in the flight direction of the aircraft. For a typical "swell-run", the aircraft heading is chosen to correspond to the vector direction of the swell (within a few degrees). The resulting spectrum is an accurate measure of the total energy on the surface if the energy is primarily contained in only one sector. Energy orthogonal to the flight vector is effectively excluded, however. In Figure 12, the laser spectrum (courtesy of D. Ross of NOAA/SAIL) is compared with the averaged pier spectrum of Figure 11 to illustrate the probable upper bound to the energy of the wave system

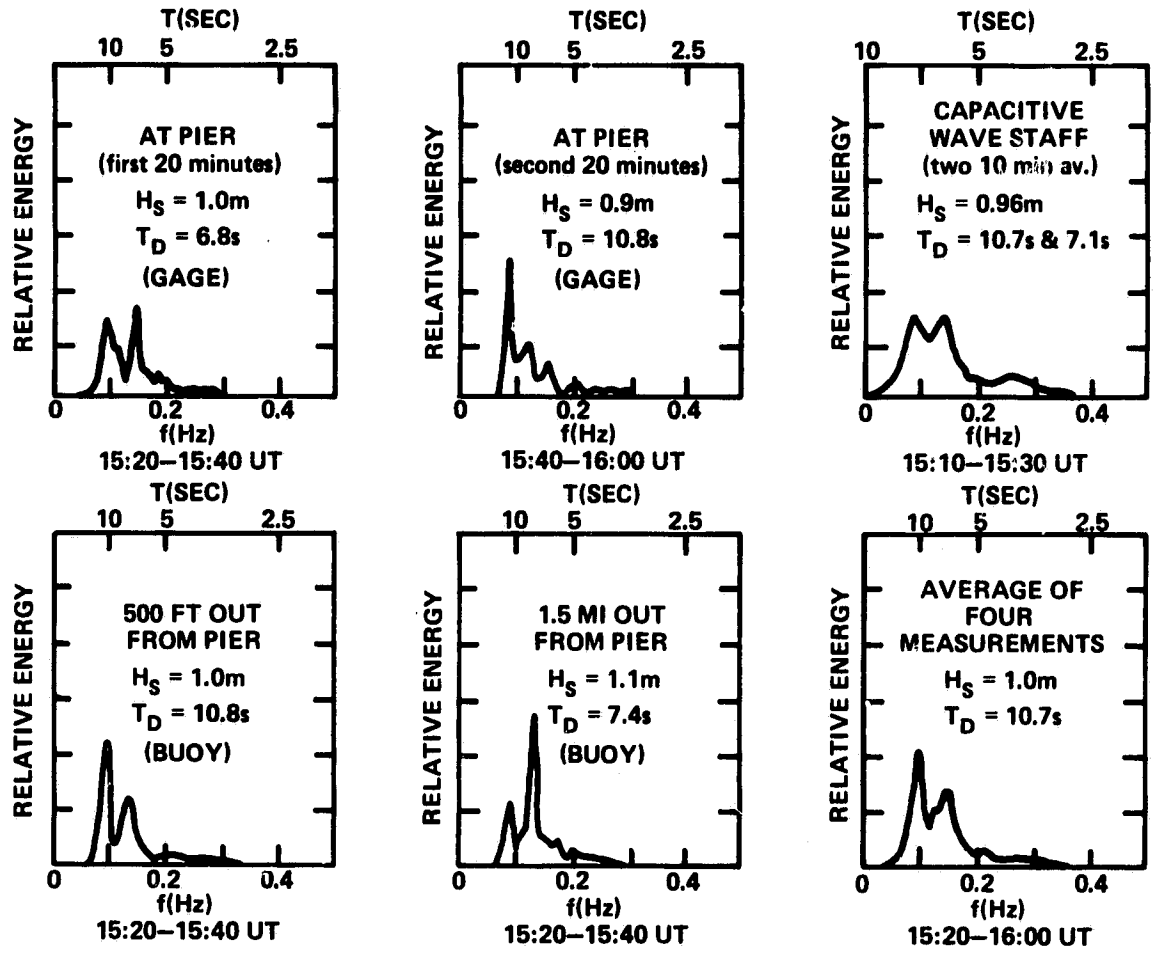

Fig. 11 Long wave spectral measurements in the vicinity of Duck during overpass of 28 Sept, 1978. (Courtesy of D. Lichy of the Coastal Engineering Research Center).

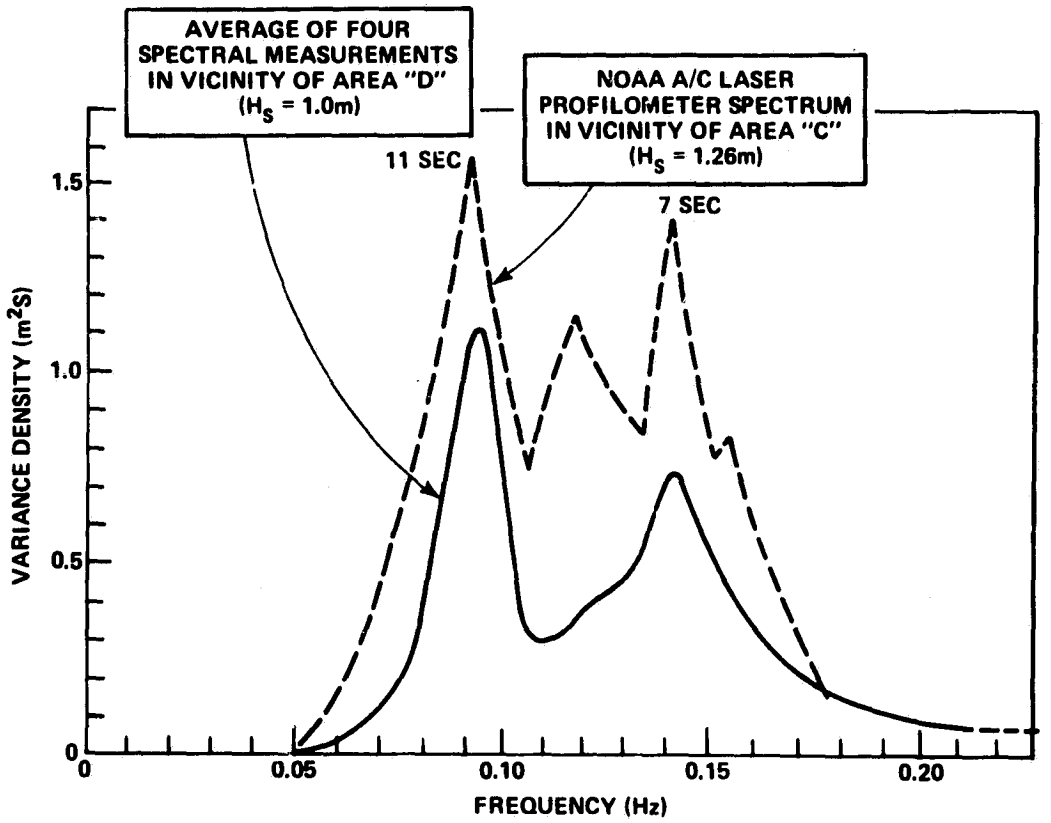

Fig. 12 A comparison of surface and air measurements of the wave height spectra in the vicinity of Duck. Laser spectrum by permission of D. Ross.

present in the area of interest. Figure 12 again verifies a double wave system at 11 seconds and 7 seconds, having total significant wave height 1.26 m, or approximately 0.9 m for each system. The energy of the 7 second system is likely underestimated due to the directional sensitivity of the laser profilometer as discussed above. The 11 second system energy, however, should be accurately indicated, and probably represents an effective upper bound to the significant wave height in the region of interest.

In summary, then, three separate measures of the 11 second system have yielded a range of significant wave height $0.4 \text{ m} < H_s < 0.9 \text{ m}$, the lower bound from FNWC, and the upper bound from the NOAA aircraft laser profilometer. The average of the four CERC pier measurements yielded an H_s equal to 0.7 m for the 11 second system.

3.4 Spacecraft SAR Measurements of the Two Dimensional Long Gravity Wave Spectrum

The spacecraft SAR was activated for approximately four minutes on 28 September as it approached the East Coast. Optically processed imagery provided by the Jet Propulsion Laboratory of the California Institute of Technology (JPL) corresponding to nearly 60 seconds of travel is shown in Figure 13. The SAR interaction wavelength is around 30 cm, and the image intensity (or reflected power) is generally proportional to the amplitude of Bragg scatterers of 30 cm wavelength on the ocean surface (Wright, 1968). The amplitude of the scatterers is strongly (but not solely) correlated with surface wind. Brighter regions of the image, in general, correspond to higher winds, and darker regions to lower winds. Figure 13 shows a large dark area which generally corresponds to very low winds. The Frontispiece is a portion of Figure 13 which has been digitally processed by JPL. Due to systematic errors in both the optically (Figure 13) and digitally (Frontispiece) processed versions, especially in the range (cross-velocity) direction, image intensity is not uniquely related to radar received power except along a given range.

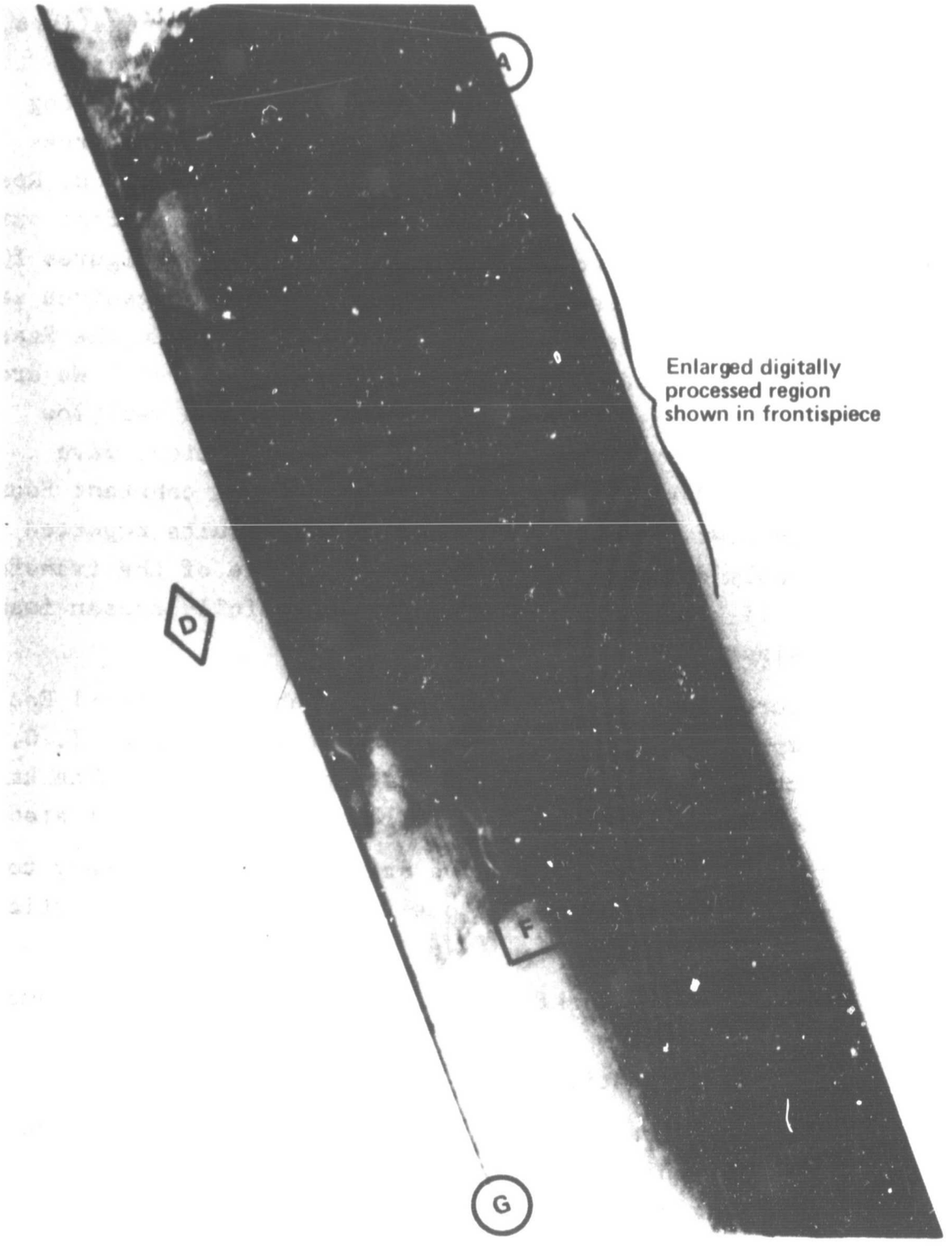

Fig. 13 Optically processed SAR imagery for 28 September from approximately 34.5° N to 37.5° N, with locations keyed to figure 10.

Wave trains may not be visible on the imagery due partly to reproduction losses. On the original high quality negatives, the presence of waves is in fact more obvious, but somewhat dependent on the observer. The higher resolution side-looking aircraft radar (SLAR) imagery, however, at least in some areas provides more convincing evidence (Figure 14, courtesy of D. Ross of NOAA/SAIL) that a strong coherent wave train does in fact exist. The SLAR imagery was collected just below location E (Figures 10 and 13), and clearly shows the presence of a highly organized wave system. The fact that waves are not clearly visible in the Seasat SAR imagery does not mean they are not present, however. We are clearly working in a near-threshold situation with a very low energy (and presumably very low backscatter modulation) wave system. Positive detection depends upon a careful coherent Fourier transformation over a large area. Successful results reported here are probably due primarily to the large size of the transform area (15 km x 15 km), and secondarily to a carefully chosen image enhancement algorithm.

Figure 15 shows a progression of enhanced optical Fourier transforms representing the image spectra at locations F, E, C, and B, respectively, as the wave trains approach shore. The transforms are the final product of the following succession of steps:

(1) a number of iterative attempts were necessary to optimize the image quality through the JPL optical processor.

(2) optical transformations were made using the same high quality JPL optical bench in a modified configuration.

(3) digitization of the transformations with an APL Optronics film reader/writer was achieved by scanning at the equivalent of 6 m ground resolution.

(4) spatial unweighted averaging to reduce noise was performed by using a 7 x 7 element sliding window.

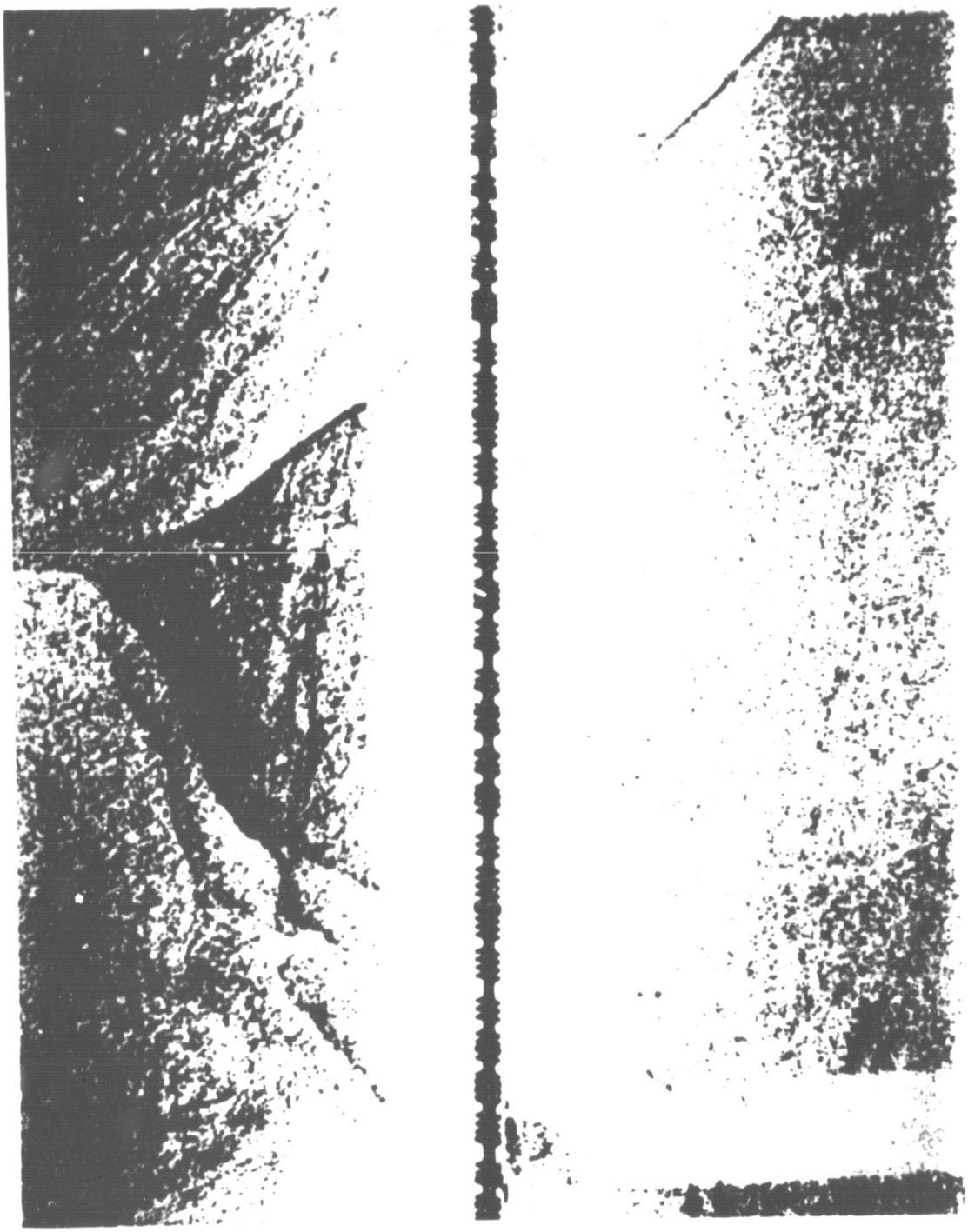

Fig. 14 Aircraft SLAR imagery taken just below location E (fig. 13), indicating the presence of a swell from the ESE. Aircraft direction of travel is within a few degrees of that of SEASAT (towards the top of the figure).

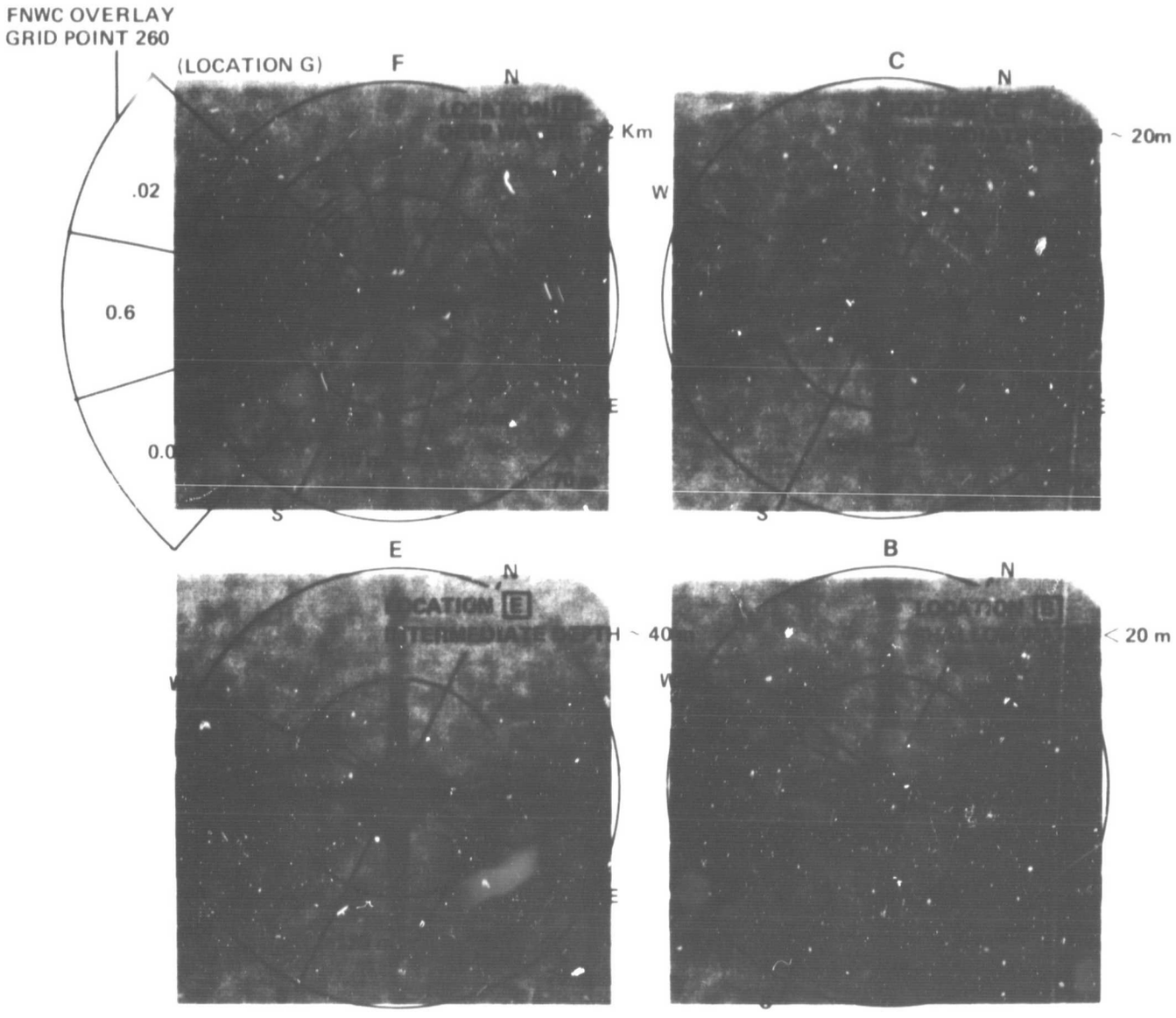

Fig. 15 Optically processed, optically transformed, and digitally enhanced SAR wave spectra from each of the four locations F, E, C, and B shown in figure 10 and 13. The sequence moves from deep to shallow water and illustrates both wave length and direction change as the 11 second swell system approaches shore. The overlay of the FNWC spectra for grid point 260 (closest available FNWC spectra) shows high correlation of the 11 second system present on Sept 28. The correlation with the 7 second system may be an artifact of the JPL optical processor. (See note added to abstract, p. vi)

(5) the filtered image was finally enhanced in contrast using a three segment piecewise linear level transformation with a very high center segment gain. Each set of break-points was individually optimized to compensate for the variations in average intensity.

The sequence shows quite clearly the refraction effects of the variations in ocean depth on the long wave component. A 210 m deep water wave at location F shortens to 170 m at E, 160 m at C, and finally to 120 m at B, in shallow water. Furthermore, the deep water spectrum F correlates well with the FNWC estimate of spectral peaks in both wave number and direction taken from location G (grid point 260). The presence of a short wave system is also apparent on the transforms. Although the SAR resolution (or at least the optical transform format) prevents locating the peak of the shorter system, the concentration of energy in that portion of the spectrum is also strongly correlated with the FNWC estimate. (However, see author's note, p. vi).

No correlation between spectral energy density and image transform density has been attempted. A proper treatment of this question would require careful accounting of the many system nonlinearities, some deliberately introduced for enhancement, and some unknown. A better understanding of ocean backscatter models is also a prerequisite for further progress here. Note, however, that the relative strengths of the short wave image spectra in the two intermediate locations are less, and the local wind also goes through a null between these two positions.

The quantitative shallow water relationship (cf Kinsman, 1965) is given in the curves of Figure 16, on which are also plotted the results of Figure 15. Each of the four center wavelengths from the optical transforms is entered on the horizontal axis of the dispersion relationship in Figure 16, and each is transformed according to the individual variation in local depth over a 15 km square area at its particular location. The process of peak location from the optical transforms is judged to have

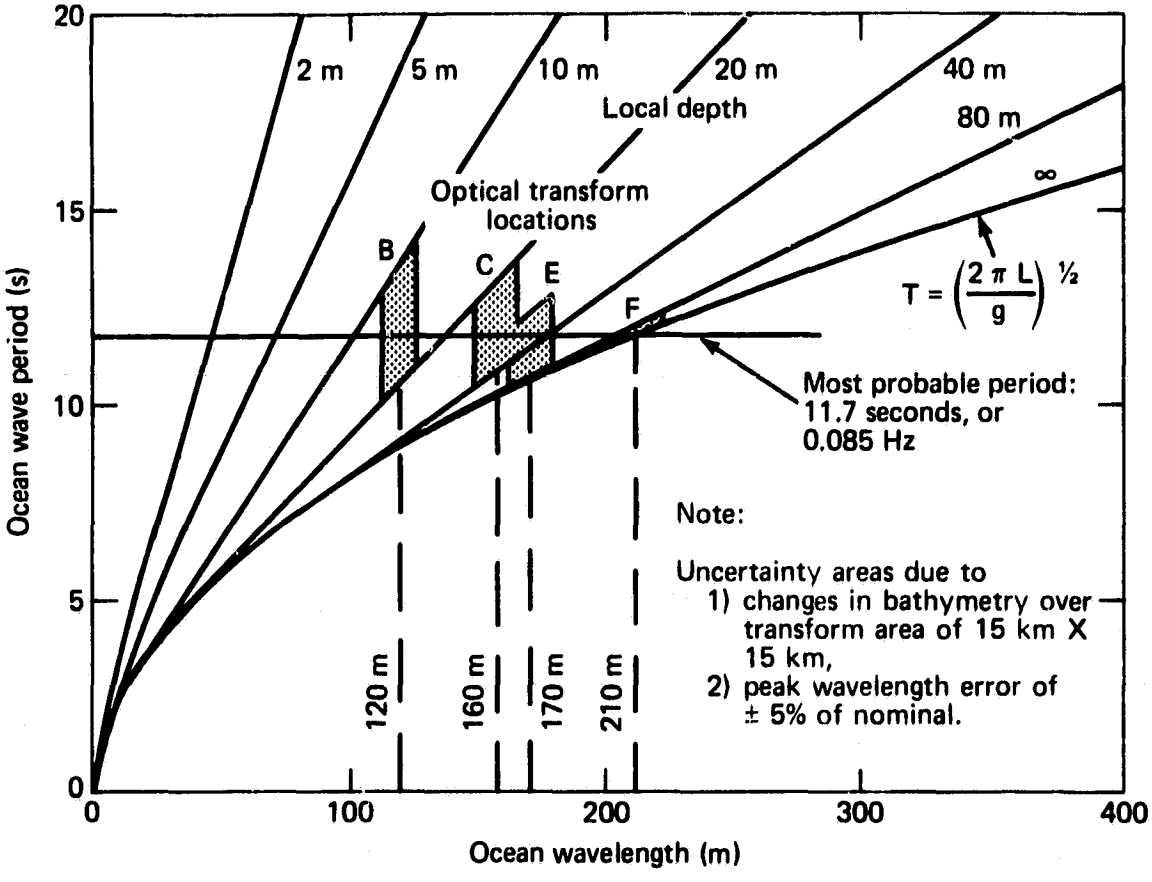

Fig. 16 The results of figure 15 plotted on the shallow water dispersion relationship.

accuracy of ± 5%. These two uncertainties combine to produce the areas of uncertainty shown in Figure 16. The data set is seen to be most consistent with the assumption of an 11.7 second swell system.

In summary, an overall comparison of all available methods for measuring wave frequency (via wavelength and bathymetry) and direction on 28 September is given in Figure 17. Wave direction for the SAR transforms was generally obtained via angular measurements made directly on the spectral plots, after having calculated true north to the nearest degree for each transform location. The variance between measurements is generally of the same order as the confidence in a particular measurement. Therefore, the data quite clearly show that for the 28 September data set, the SAR measured ocean wavelength and direction as well as any of the alternate techniques available on that day. It is possible that, in terms of separating swell systems in a mixed ocean, its accuracy may exceed that of any other existing system.

4.0 PRELIMINARY SENSOR INTERCOMPARISON FOR 28 SEPTEMBER

4.1 Motivation

Aside from the accurate monitoring of ocean wavelength and direction with the SAR, there are a number of additional questions that can be addressed by looking at the SAR imagery in the context of the simultaneous data available from the other Seasat sensors. This section of the paper will specifically treat

(1) the relationship between average radar backscatter power from the SAR (at L-band) and the Seasat scatterometer (SASS) derived winds (at K-band), and

(2) a preliminary assessment of the Seasat composite summary of 28 September compared with the FNWC estimates.

LOCATION	SOURCE	FREQUENCY (Hz)		WAVE DIRECTION (DEGREES)	
		SPECTRAL PEAK	DEVIATION	MEAN	DEVIATION
A	FNWC	0.086	–0.002	279°	–4°
B	S/C SAR	0.084	–0.004	283°	0°
C	S/C SAR	0.086	–0.002	287°	+4°
C	A/C LASER A/C VISUAL	0.091	+0.003	280°	–3°
D	WAVE GAGE GND RADAR	0.092	+0.004	292°	+9°
D	A/C SLAR	NOT REDUCED		287°	+4°
E	S/C SAR	0.088	0.000	280°	–3°
F	S/C SAR	0.084	–0.004	285°	+2°
G	FNWC	0.092	+0.004	274°	–9°
MEAN/RMS DEV		0.088	0.003 or 3.5%	283°	5.1°

Fig. 17 Measurement summary for 28 Sept.

4.2 SAR Backscatter versus SASS-Derived Wind

The SASS wind field can be extracted from NASA/Langley Research Center (LaRC) computer print-outs of the SASS wind vector analysis provided by E. M. Bracalente (1979). The wind vector profile along the "line of interest" is shown in Figure 22. This line corresponds to a SASS incidence angle of 25° to 27° (fore and aft beams at 45°). The resulting wind vector magnitude profile is shown in Figure 18, and has error bars of ± 2 m/s, corresponding to the present level of confidence in SASS wind magnitude accuracy (Seasat GOASEX I report, 1979). The wind circulates around the trough located at about 31°N, and flows within 11° of north from 33.5°N to at least 36°N. A local maximum of ~14 m/s occurs just below 34°N, and reduces to less than 5 m/s by 36°N. The line of interest therefore contains at least a factor of three range of wind magnitudes, and by considering only that range between 33.5°N and 36°N, the wind direction is always within 11° of North. Anisotropic features of the wind field will therefore have little effect on the data in this range.

The SASS does not attempt to predict winds lower than ~2.5 m/s, so the extrapolation to zero winds on Figure 18 actually results from a separate location of the minimum SASS backscatter. Also, the profile shown in Figure 18 contains considerable smoothing, which may introduce errors below about 5 m/s. Nevertheless, the SASS clearly shows a relatively smooth, monotonically changing wind field which forms the basis for the SAR/SASS comparison. Note the values of the FNWC estimates (triangles), also plotted on Figure 18. In all cases they are lower than the SASS, and possibly because of course sampling, would give a much different impression of the local wind profile.

The optically processed SAR imagery provided by JPL is accompanied by a calibrated noise wedge which is stepped in precise 3 dB intervals at the input to the optical processor. Such a scheme, although not as precise as a noise wedge introduced at the spacecraft instrument input, nevertheless allows the elimination

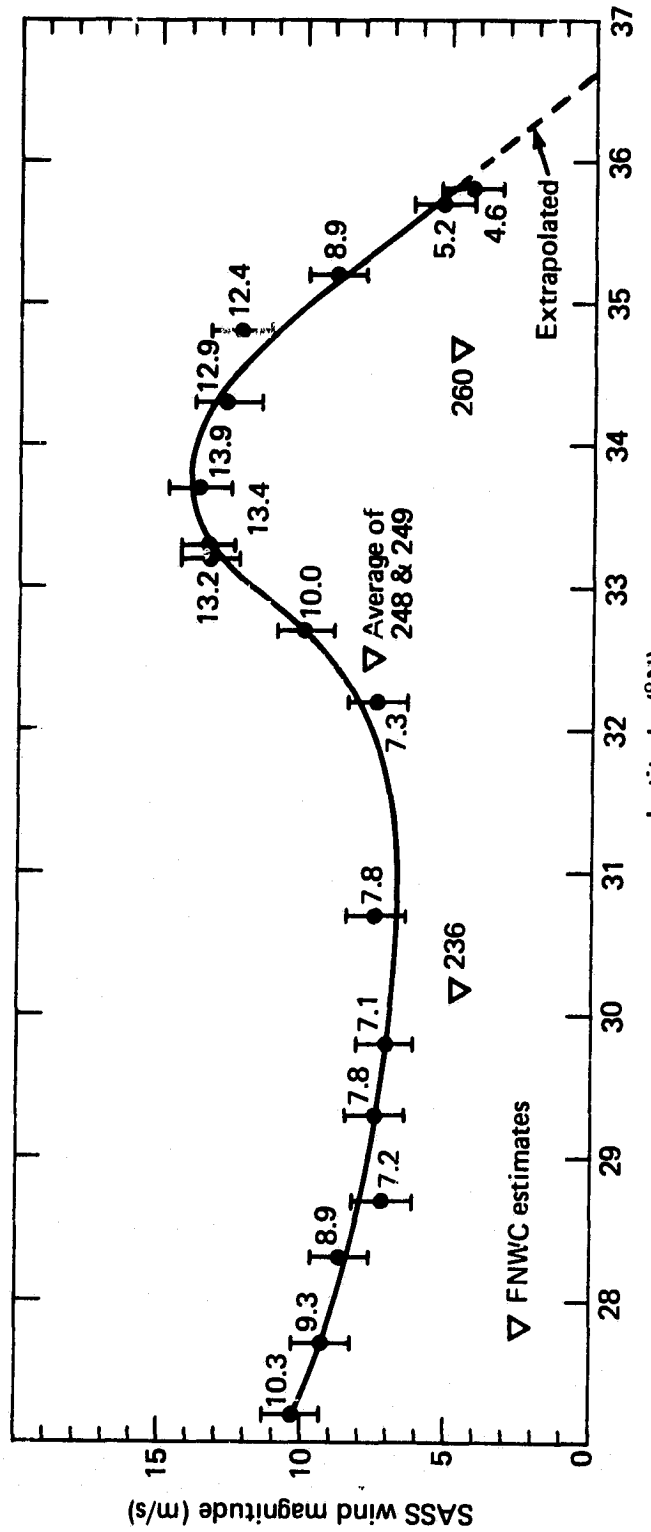

Fig. 18 SASS wind magnitude vs latitude along line of interest.

of the most non-linear and uncontrolled portion of the end-to-end system, i.e., the optical processor and film development.

Figure 19 contains the graphical analysis which allows the mapping of surface wind magnitude as measured by the SASS into input power as measured by the SAR. The figure contains a smoothed and unsmoothed profile of the SAR image negative density plotted on the same coordinates with the smoothed SASS wind field from Figure 18. Even with the caveats on the SASS profile below 5 m/s mentioned above, the overall correlation is apparent. Also plotted on a common density axis is the SAR noise calibration curve, corresponding to input power levels shown on the axis to the upper right of the figure.

A series of three entries is made on the vertical SASS wind magnitude axis, corresponding to winds of 14 m/s, 7 m/s, and 3.5 m/s. These entries are reflected off the SASS wind curves at the appropriate latitudes, through the SAR smoothed density curve, and finally through the SAR power-to-film-density calibration curve. Each input SASS wind is therefore transferred to a corresponding SAR relative input power.

Figure 19 shows that 3 dB changes in SASS wind appears to result in SAR input power changes of between 1.5 and 2 dB. This final relationship is plotted in Figure 20, and indicates reasonable agreement with a power law dependence of 0.5 to 0.65. This result is in agreement with results of Weissman, et al. (1979), who calculate a power law dependence of 0.58 from aircraft L-band measurements of Hurricane Gloria.

4.3 The Composite Seasat Summary in the Context of FNWC Estimates for 28 September

Even though the FNWC SOWM cannot be considered a primary standard, it represents a data base which contains the best available knowledge of worldwide wind and wave conditions. FNWC, using a variety of ship and station reports, inserts them into a wind-driven wave generation model, and produces a global wind field and

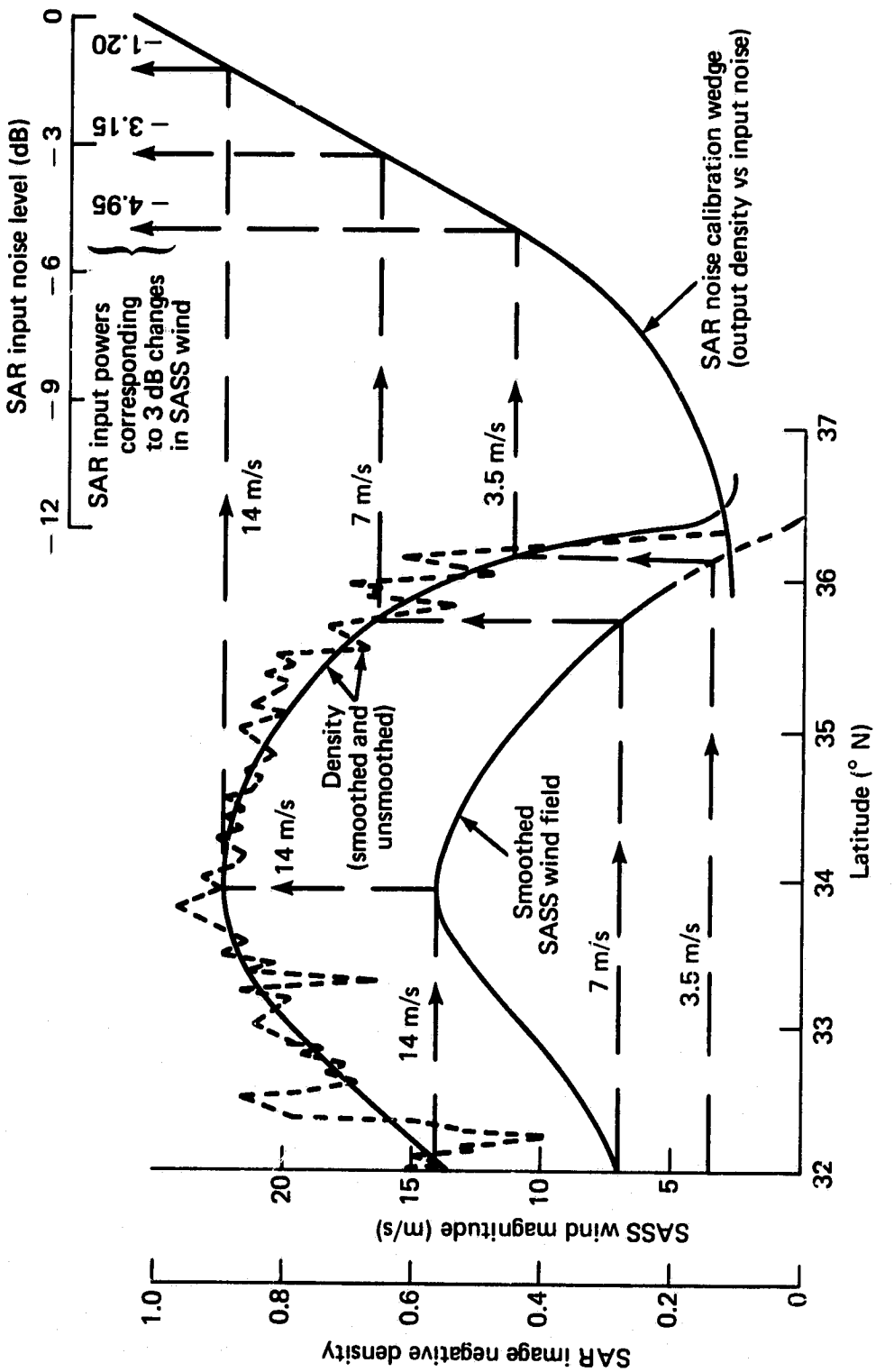

Fig. 19 Graphical analysis relating SAR backscatter to SASS wind field

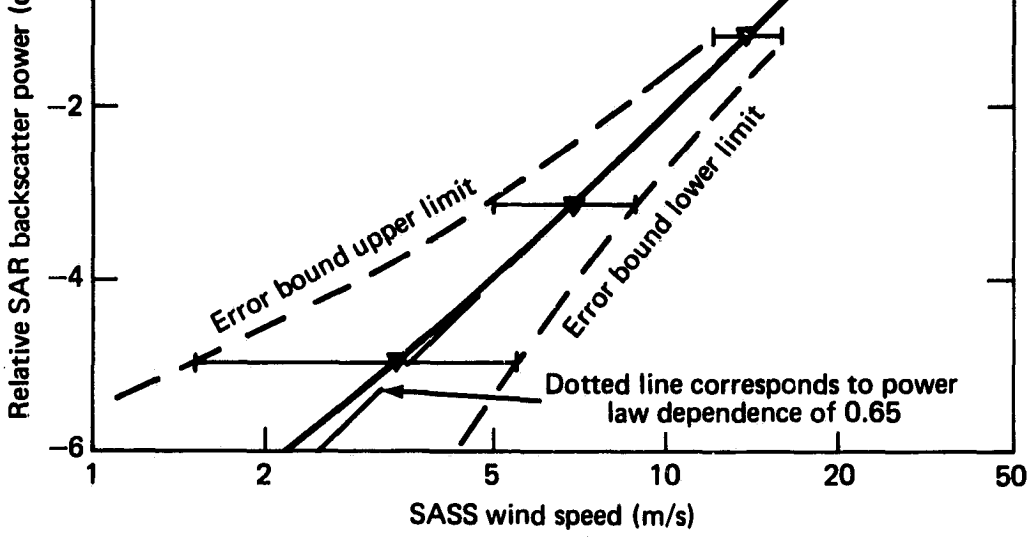

Fig. 20 Results of graphical analysis plotted in figure 19.

sea state every six hours. The Seasat data set for 28 September lends itself well to a comparison with the FNWC model, since both the wind and waves exhibit local maxima in the region of interest.

Figure 21 shows the Seasat altimeter wave height measurements along the subtrack shown in Figure 22. The on-board-processed data points have been rescaled on the right margin employing corrections generated by G. S. Hayne (1979) using a more sophisticated algorithm and comparisons with in-situ data. The residual bias should be less than 0.25 m. Several secondary peaks in H_s are apparent at latitudes just to the south of the major peak of 3 m at 33.2°N.

Figure 22 is a composite of much of the significant information from both FNWC and Seasat. In particular, it displays the wind and wave profiles as measured by the Seasat SASS and altimeter, respectively. The low pressure trough and the approaching front (see Figure 1) are shown, although the trough axis has been slightly realigned to achieve consistency with the scatterometer wind field. Also, for reference, four relevant FNWC grid points are shown along with the FNWC significant wave height contours around the local maximum. Two of the grid points shown are chosen because they represent the positions of the highest local wind speeds in the area, according to the FNWC model.

Here we can begin to see some of the subtle differences between "conventional" sources and potentially available satellite systems. FNWC, perhaps due to the courseness of the grid system, appears to be hindcasting peak winds which are not only low in magnitude (~8 m/s versus ~14 m/s from Seasat), but are offset by more than one degree in latitude from those measured by Seasat. This inaccuracy is perhaps trivial for the intended users of FNWC data. Nevertheless, the major point to be made is the scale of the global monitoring potentially available from space.

The discrepancy between the present FNWC model and Seasat measurements are further reinforced in the significant wave height distribution predicted by each. As Figure 22 (left-hand portion)

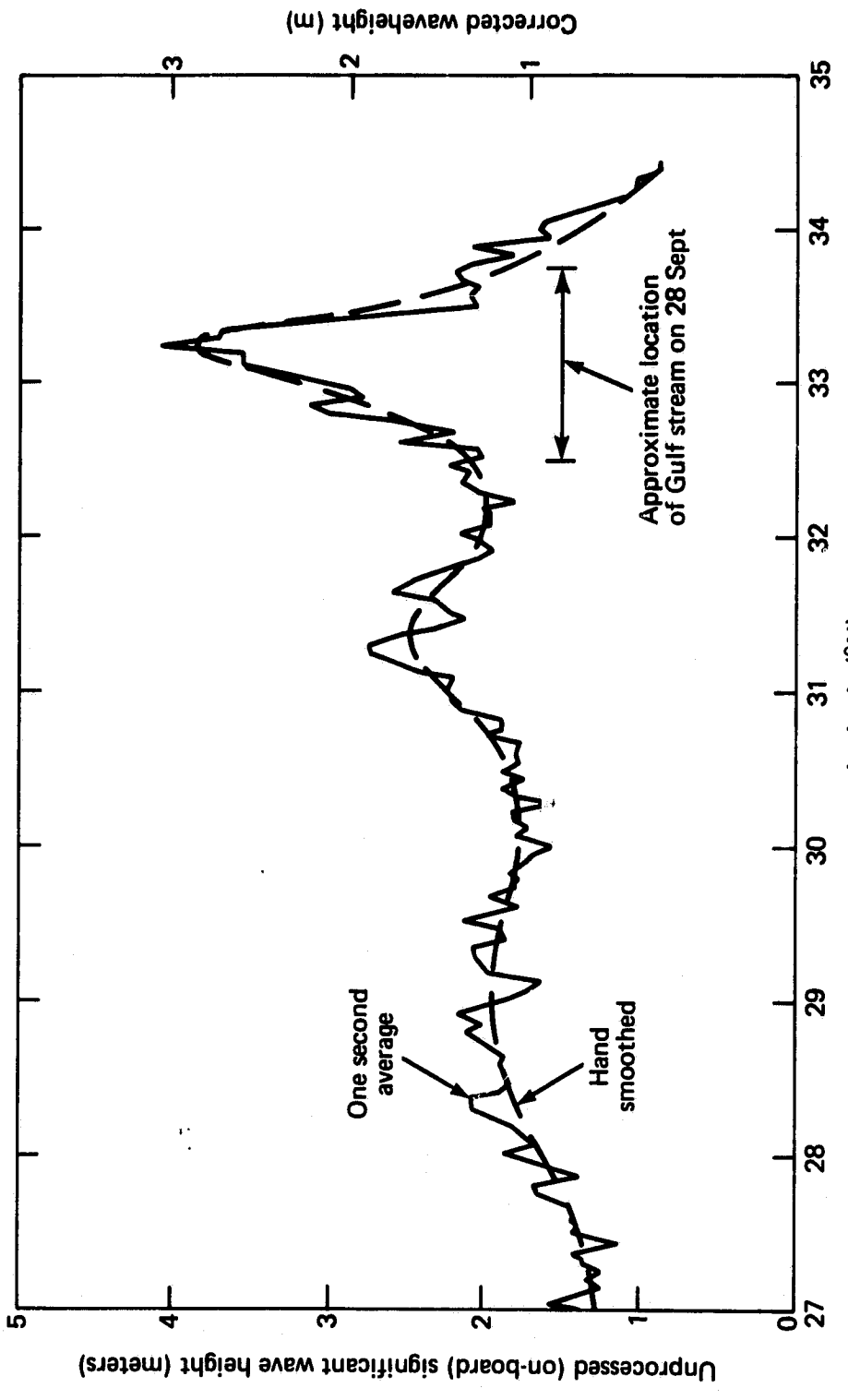

Fig. 21 Significant wave height profile along SEASAT altimeter subtrack, 15:18:22 GMT to 15:20:35 GMT, 28 Sept, 1978.

x3

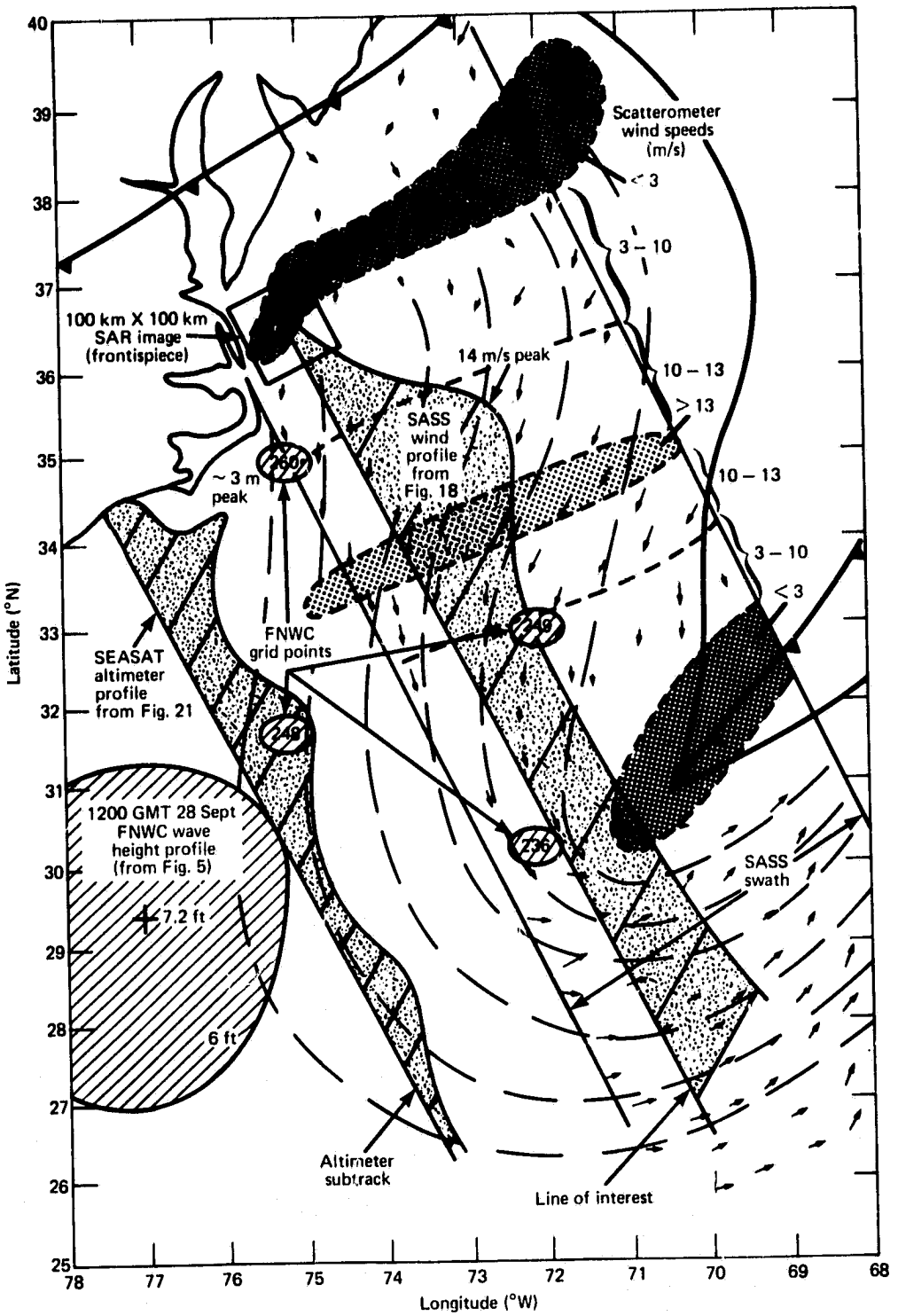

Fig. 22 Composite profile of SEASAT wind and wave measurements 28 September, 1978.

shows, the discrepancies in wind are at least partially translatable to discrepancies in waves. The FNWC model predicts a local maximum in H_s which is apparently both too low in energy and too far south. The half-amplitude peak measured by Seasat is on the order of one degree in latitude. In addition to the displaced wind field effects, we may be seeing a wind interaction with the Gulf Stream, whose position coincides with the peak wave height region as measured by the altimeter. The FNWC peak (see Figure 8) is much broader, as one would expect from a smoothed wind field input, but is also displaced.

There is no intent here to criticize the FNWC model, nor is it likely that this present comparison would come as a surprise to FNWC users. This discussion is merely an attempt to illustrate the scale and self-consistency of wind and wave measurements that could be made worldwide with a satellite of proper configuration. Furthermore, knowledge of the wave spectra, not only in deep water, but in near-shore areas, appears to be possible with SAR. Even the straight-forward measurement of predominant wavelength and direction described in Section 3 of this report would provide a powerful self-check of wind-generated wave spectra. This self-check, in deep ocean at least, might require a substantially different coverage pattern than existed on Seasat, and might be designed to utilize much less channel bandwidth than Seasat required. The optimum instrument configuration, of course, depends upon a proper weighting of (presently ill-defined) user needs, and therefore cannot be further addressed here.

4.4 Conclusions

Synoptic monitoring of the wind and waves may best be done with one single instrument which optimally combines the best features of each of the previously separate ones. An imaging mode quite clearly will yield useful information, and such a mode should be seriously considered as part of this future instrument. Substantial creativity is needed, however, to synthesize an efficient, low cost, and scientifically useful combination. It is also vital

that the instrument configuration remain sensitive to our growing, but as yet incomplete, knowledge of the behavior of the composite ocean wave spectrum, in particular, the interaction between the short Bragg scatterers and the parameters which we seek to monitor: wind, long waves, currents, and surface films.

Particular efforts which are recommended for substantial long term support are:

(1) experiments to understand the mechanics of radar scatter, especially wave-wave and wave-current interactions,

(2) exhaustive analysis and intercomparisons of the large bank of existing Seasat data, both with conventional sources and between spacecraft instruments, and

(3) a system study which carefully synthesizes both (1) and (2) into a new experimental (as opposed to operational) instrument that has both maximum scientific utility and managable data handling.

5.0 REFERENCES & NOTES

Beal, R. C., J. Springett, R. Lipes, C. Wu, and N. Evans, "Seasat A SAR Design Verification Report", JPL Technical Report 622-31 (August 15, 1977).

Beal, R. C., "Useful Spaceborne Synthetic Aperture Radars", XXIXth International Astronautical Federation Congress Proceedings, Dubrovnik, Yugoslavia (1978) (in press).

Bracelente, E. M., data provided during the GOASEX II Workshop, Pasadena, California (25-29 June 1979).

Brown, W. E., Jr., C. Elachi, and T. W. Thompson, "Radar Imaging of Ocean Surface Patterns", Journal of Geophysical Research, 81, No. 15 (1976).

Elachi, C., "Wave Patterns Across the North Atlantic on September 28, 1974, from Airborne Radar Imagery", Journal of Geophysical Research, 81, No. 15 (1976).

Elachi, C. and W. E. Brown, "Models of Radar Imaging of Ocean Surface Waves", IEEE Trans. Antennas and Propagation, AP-25 (1977).

Gonzalez, F. T., R. C. Beal, W. E. Brown, P. S. DeLeonibus, J. F. R. Gower, D. Lichy, D. B. Ross, C. L. Rufenach, J. W. Sherman III, R. A. Schuchman, "Seasat Synthetic Aperture Radar: Ocean Wave Detection Capabilities", Science, 204 (29 June 1979).

Hayne, G. S., of Applied Science Associates, via private communication with E. Walsh. The algorithm is similar to one developed by L. Fedor.

Jordan, R., "The Seasat-A Synthetic Aperture Radar Design and Implementation", Proceedings of the Synthetic Aperture Radar Technology Conference, Las Cruces, N.M. (8-10 March 1978).

Kinsman, B., "Wind Waves, Prentice Hall, pp 126-133 (1965).

Lazanoff, S. M. and N. Stevenson, "An Evaluation of a Hemispheric Operational Wave Spectral Model", FNWC Technical Note 75-3, Monterey, Calif. (1975).

Lichy, D., data collected by the CERC facility at Duck, N.C.

Mason, C., "Coastal Engineering Research Center's Field Research Facility at Duck, N.C.", Shore and Beach, 47, No. 2 (April 1979).

Ross, D. and V. J. Cardone, "Laser Observation of Wave Growth and Foam Density for Fetch Limited 23 m/s Winds", Hydrology and Oceanography, Third Annual Earth Resources Program Review, Vol. III (1970).

Seasat Gulf of Alaska (GOASEX I) Workshop Report, JPL Technical Report 622-101 (April 1979).

Shuchman, R. A., E. S. Kasischke, and A. Klooster, "Synthetic Aperture Radar Ocean Wave Studies", Final Report 131700-3-F, Environmental Research Institute of Michigan, Ann Arbor (1978).

Teleki, P. G., R. A. Shuchman, W. E. Brown, Jr., W. McLeish, D. B. Ross, and M. Mattie, "Ocean Wave Detection and Direction Measurements with Microwave Radars", Proceedings of the Oceans '78 Conference, Washington, D. C. (8 September 1978).

Weissman, D. E., D. B. King, and T. W. Thompson, "Relationship Between Hurricane Surface Winds and L-Band Radar Backscatter from the Sea Surface", to be published in Journal of Applied Meteorology (Aug 1979).

Wright, J. A., "A New Model for Sea Clutter", IEEE Trans. Antennas and Propagation, AP-16, No. 2 (March 1968).

THE JOHNS HOPKINS UNIVERSITY
APPLIED PHYSICS LABORATORY
LAUREL MARYLAND

Appendix

THE SEASAT SYNTHETIC APERTURE RADAR EXPERIMENT

I. INTRODUCTION

Much of the continuing climatic change which affects our lives, both from day to day, and from century to century, is bound up in the vast amounts of energy constantly being transferred from the atmosphere of our planet to its oceans and back again. Global trade winds and an uneven solar flux create large scale oceanic currents and significant temperature gradients which influence world climate and even control human migration patterns. The Gulf Stream, for example, continuously carries heat from the Caribbean to the seas of Northern Europe, and fosters the only large scale human settlements occurring closer to a pole than to the equator.

Civilian space programs are increasingly justified on their applications potential, in particular their ability to demonstrate clear economic or social benefit. Communication satellites have been the most successful in this regard, as measured by the degree of federal subsidy necessary for their survival. Navigation and weather satellites each have an increasing array of private users, but continue to be primarily funded by the government. Most of them are, however, managed by "user agencies", and are therefore termed "operational". For a satellite system to become operational is a significant event, since it implies that at least one user agency is sufficiently convinced of its benefit to provide primary sponsorship. (The Departments of Commerce, Interior, and Agriculture are examples of user agencies; NASA is not.)

We are currently in the midst of a several decade evolution during which high resolution images of our planet taken routinely from space are dramatically expanding our environmental sensitivity. The operational weather satellites have been monitoring global cloud movement for several years. The near-operational LANDSAT's are beginning to provide accurate estimates of some global resources, the most notable progress being an annual inventory of

the global wheat crop. Last year an experimental microwave imaging radar was launched as part of the oceanographic satellite, Seasat-A, and an entirely new region of the spectrum for monitoring our planet was opened.

In many respects, microwave imagery obtained from orbit is a complement to visible imagery, and provides information not otherwise available. Its high resolution is obtained by artificially synthesizing an aperture many kilometers long in space (thus the name synthetic aperture radar, or SAR), and as a result it is both sophisticated and expensive. The SAR does, however, have two elementary advantages over any other high resolution sensor: it can collect imagery through cloud cover and without the help of the sun. In addition, the SAR has the proven ability to map the details of the polar ice fields, and the potential (but not proven) ability to unconditionally image ocean swell. These are, in fact, two of the primary reasons for placing the instrument on an oceanographic satellite. The benefits to transoceanic shipping, severe weather prediction, and long range climatology can be substantial if the SAR measures either ice fields or wave fields reliably. Conversely, one or the other of these applications will probably have to be conclusively demonstrated if the SAR is to obtain operational status on any future oceanographic satellite.

Having briefly stated some rationale for SAR in space, this appendix will deal with:

(1) the concept of aperture synthesis,
(2) extension to the range dimension, and
(3) the 98 day Seasat SAR experiment.

II. APERTURE SYNTHESIS

The angular resolution of any transmitting or receiving system, including a synthetic aperture radar, is ultimately limited by the size of its aperture, according to classical diffraction theory. Expressed simply,

$$\phi = 1/n \qquad (1)$$

where

ϕ = the angular resolution in radians
n = the size of the aperture, expressed in wavelengths.

When the same aperture is used for both the transmitter and receiver of energy, as it is in the SAR, then the resulting angular resolution ϕ' is effectively halved ($\phi' = \phi/2$). Now imagine the satellite geometry shown in Figure A-1, typical of the Seasat SAR parameters, orbiting at altitude (or slant range, for near-nadir geometry) $h = 10^6$ m, and containing a SAR operating at radar wavelength $\lambda = 0.2$ m. The length of the synthetic aperture L is related to the ground resolution in the flight direction of the spacecraft (conventionally referred to as azimuth resolution), r_a, by

$$r_a = \phi' h = \frac{\lambda}{2L} h \ . \qquad (2)$$

An azimuth ground resolution of 6 m requires a synthetic aperture length of 16 km. A satellite traveling at this altitude has orbital speed about 8 km/sec, and therefore requires about two seconds to synthesize the required aperture.

Notice that the length of the real aperture on the spacecraft has not entered explicitly into the equations. However, the real aperture must be sufficiently short to allow a particular point on the ground to remain entirely within the beam during the aperture synthesis interval. This leads to the relationship (again illustrated in Figure A-1)

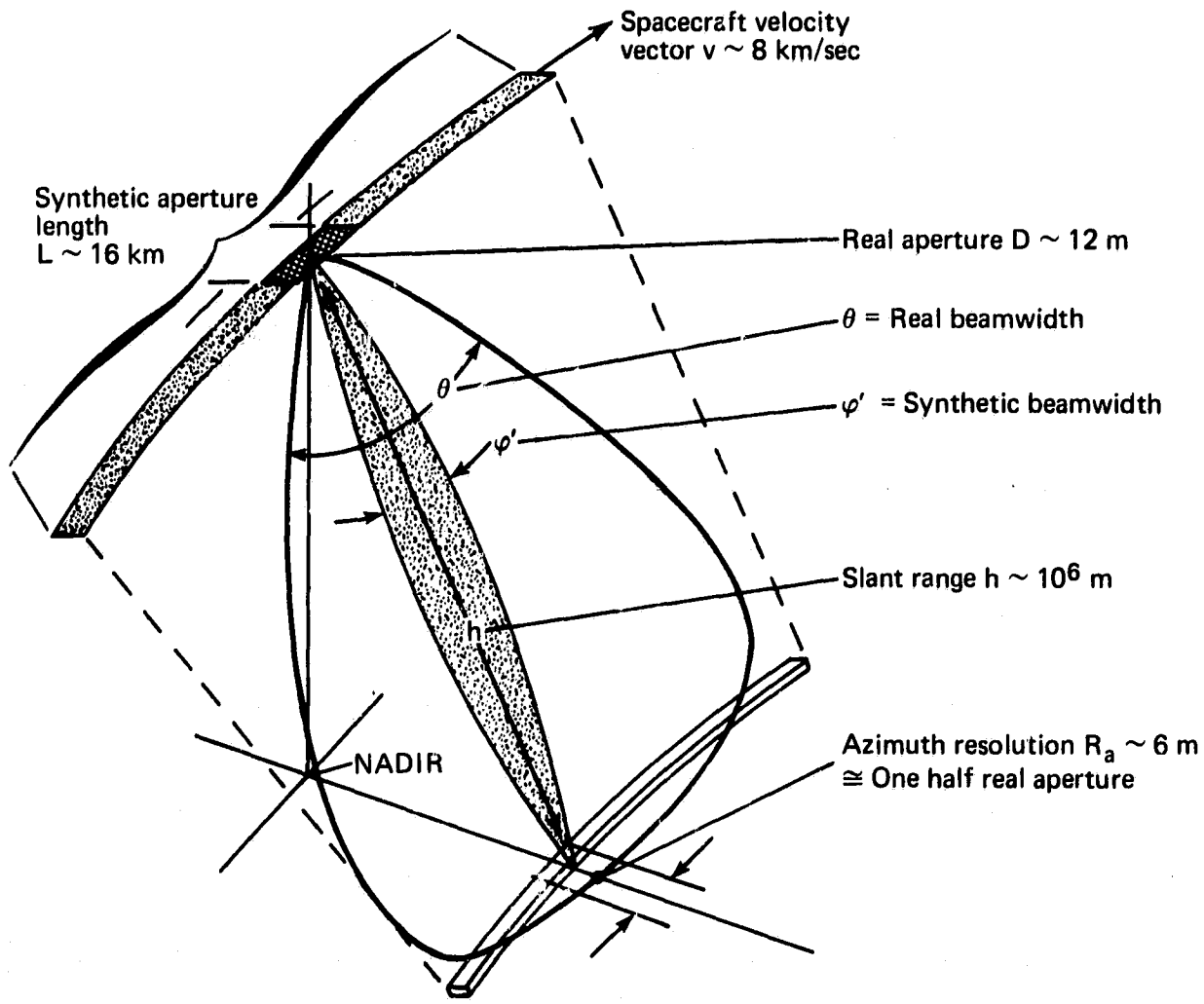

Fig. A1 Ultimate resolution of a synthetic aperture.

$$L = h \frac{\lambda}{D} . \tag{3}$$

where D is the real aperture length, and L, h, and λ have been defined above. Combining (2) and (3) leads to the fundamental lower limit for resolution

$$r = D/2 . \tag{4}$$

Therefore, if a ground resolution of 6 m is desired, the real aperture can be no longer than 12 m to maintain a point in the real beam for a sufficiently long time. The resolution limit is independent of range since the time over which a particular point is illuminated increases with range, thus allowing a correspondingly larger synthetic aperture to be formed. The Seasat SAR had a real aperture length D = 12 m, and so was theoretically capable of 6 m azimuth resolution, assuming the maximum allowable synthetic aperture of 16 km could be constructed. Although 6 m azimuth resolution from Seasat is theoretically possible, the imagery is typically processed to yield only 25 m. That is, only 4 km of synthetic aperture, or 0.5 second of data is processed at a particular instant of time. Any 4 km from the total 16 km length will satisfactorily produce 25 m resolution. Moreover, since the predominant system noise in the SAR is due to "coherent speckle" which tends to be Rayleigh-distributed in amplitude (i.e., there are wide variations in the reflected signal from a resolution element as the illumination angle is slightly varied), each 4 km segment potentially allows an independent sample of the "average" reflectivity distribution. Therefore, the variance within a scene can be considerably reduced by separately processing and combining four independent 25 m images.

So far our discussion has dealt only with the very basic criteria for obtaining high (azimuth) resolution along the velocity vector of the satellite. We have not examined the actual mechanics of collecting and processing the information to reform the image,

nor have we expanded our discussion to include the orthogonal (range) dimension. It should be apparent, however, that the synthetic aperture must be constructed with extreme care to fully realize its potential. For example, the resolution suffers if the satellite is perturbed from the perfect trajectory by a significant fraction of its operating wavelength (say, 5 cm) as it traces out the 16 km aperture. This is equivalent to forming an image in a camera with a scratched or distorted lens. Various types of aberrations can occur, all of which lead ultimately to loss of resolution and contrast in the image.

Having explored some of the fundamental requirements for aperture synthesis, Figure A-2 schematically summarizes the major steps in image formation in terms of a point source, or impulse response. Because an imaging system must be linear to first order, superposition arguments can extend the result to an arbitrary distribution of radar backscatter. A point source (step 1) having been illuminated by a coherent radar, emits a series of concentric wavefronts (step 2). The emission occurs, of course, only while the point source is within the aperture beam, as discussed above. The spacecraft cuts through the concentric wavefronts (step 3), and the SAR receiver intercepts an energy flux which varies with position (or time) as the wavefronts are traversed (step 4). This wavefront record is called by several names: it may be the doppler or phase history for radar engineers, or it may be the hologram, diffraction pattern, or one dimensional zone plate for those more optically inclined. The essential point is that this wavefront record, containing a complete phase and amplitude history of the point source for the entire synthetic aperture interval, is all that is required to reproduce a diffraction limited version of the original point source.

The wavefront record is transferred from the spacecraft to any of several ground stations through a data link (step 5), where it is recorded on some storage medium, usually digital tape or optical film. For Seasat, the record was normally recorded on

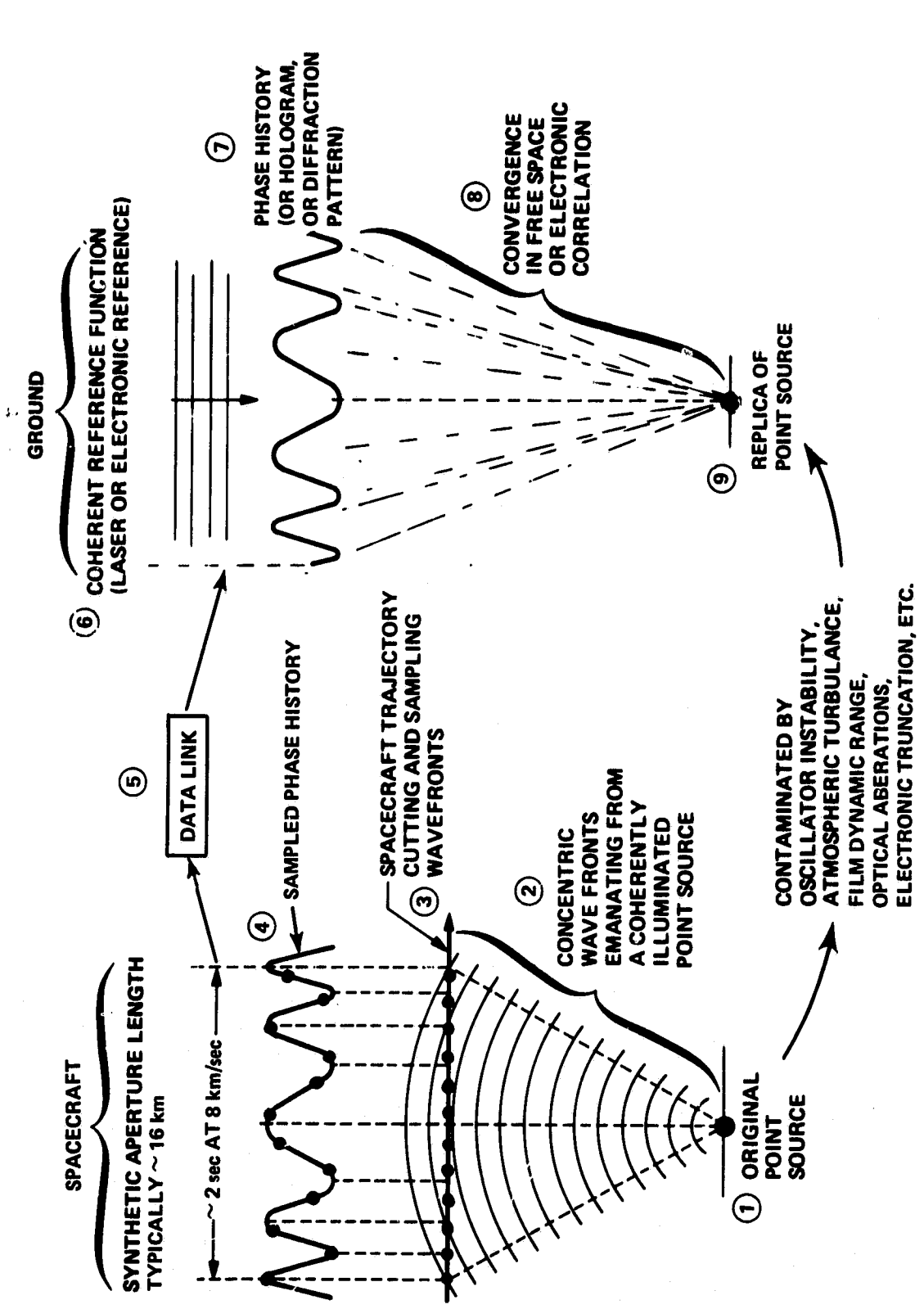

Fig. A-2 Construction of a synthetic aperture

tape at the station, and later transferred to film at a central facility. To reproduce the point source from the wavefront record, a coherent reference function (step 6) such as plane waves from a laser impinges upon the phase history (step 7). The phase history, being essentially the diffraction pattern of a point source, causes a lensless convergence of the plane waves in free space (step 8) to form a replica of the original point source, thus completing the cycle.

In practice, there are several variations to the simple scheme described in Figure A-2, some helpful, some annoyances, and others irrevokably destructive. A simple lens inserted at step 8 shortens the convergence distance, and so is a help. On the other hand, the spacecraft trajectory (step 3) is better described by an arc of varying center of curvature than by a straight line. Thus, the diffraction pattern becomes a function of time, which is clearly an annoyance requiring an adaptive processing strategy. Atmospheric turbulence, reference function instabilities, and lens aberations are representative of destructive and basically uncorrectable contamination sources. Much of the effort and expense of the Seasat SAR can be directly attributed to the need to account for the systematic contamination sources, and to minimize the random ones.

III. EXTENSION TO TWO DIMENSIONS

The extension of SAR image formation to the range (cross-velocity) direction is straightforward, but places strict timing and synchronization requirements on the design, and severely restricts the total range interval (or corresponding ground swath width) that can be accommodated. Range information is possible in a SAR only because the synthetic aperture need not be continuous, but may be constructed with samples; that is, the transmitter may be pulsed. It is sufficient that one pulse be transmitted each time the real aperture moves by one half its length. This is called "filling the aperture", and leads to a maximum time interval $\tau = D/2v$ during which range information can be collected. For $D \sim 12$ m and $v \sim 8$ km/s, $\tau = 750$ μs. In actual practice, the aperture is slightly "overfilled" to reduce the possiblity of spurious signals that could reduce contrast. The Seasat SAR, for example, typically operates at an interpulse period of 600 μs. Moreover, somewhat less than half of this time interval represents signal of sufficient quality to produce good imagery.

Figure A-3 shows the synchronization constraints imposed by the Seasat geometry. Transmitter pulses are emitted every 600 μs in the cross-track direction, 20° away from nadir. These pulses form concentric expanding rings of energy with separation of about 200 km ($c\tau = 3 \times 10^{8}$ m/s $\times$ 600 $\times 10^{-6}$ s $\simeq$ 200 km). With the satellite orbiting at an altitude of 800 km, there are always four such pulses descending at any time. Since the antenna illuminates only that region around 20° from nadir, no significant backscatter occurs except at a slant range around 850 km. This is no accident, since the round trip distance of 1700 km must be chosen to allow the return from a particular pulse to occur exactly between two subsequently transmitted pulses. The geometry and pulse interval for the Seasat SAR are chosen to allow the return from a given pulse to occur exactly midway between the eighth and ninth subsequent pulses. As Figure A-3 shows, the

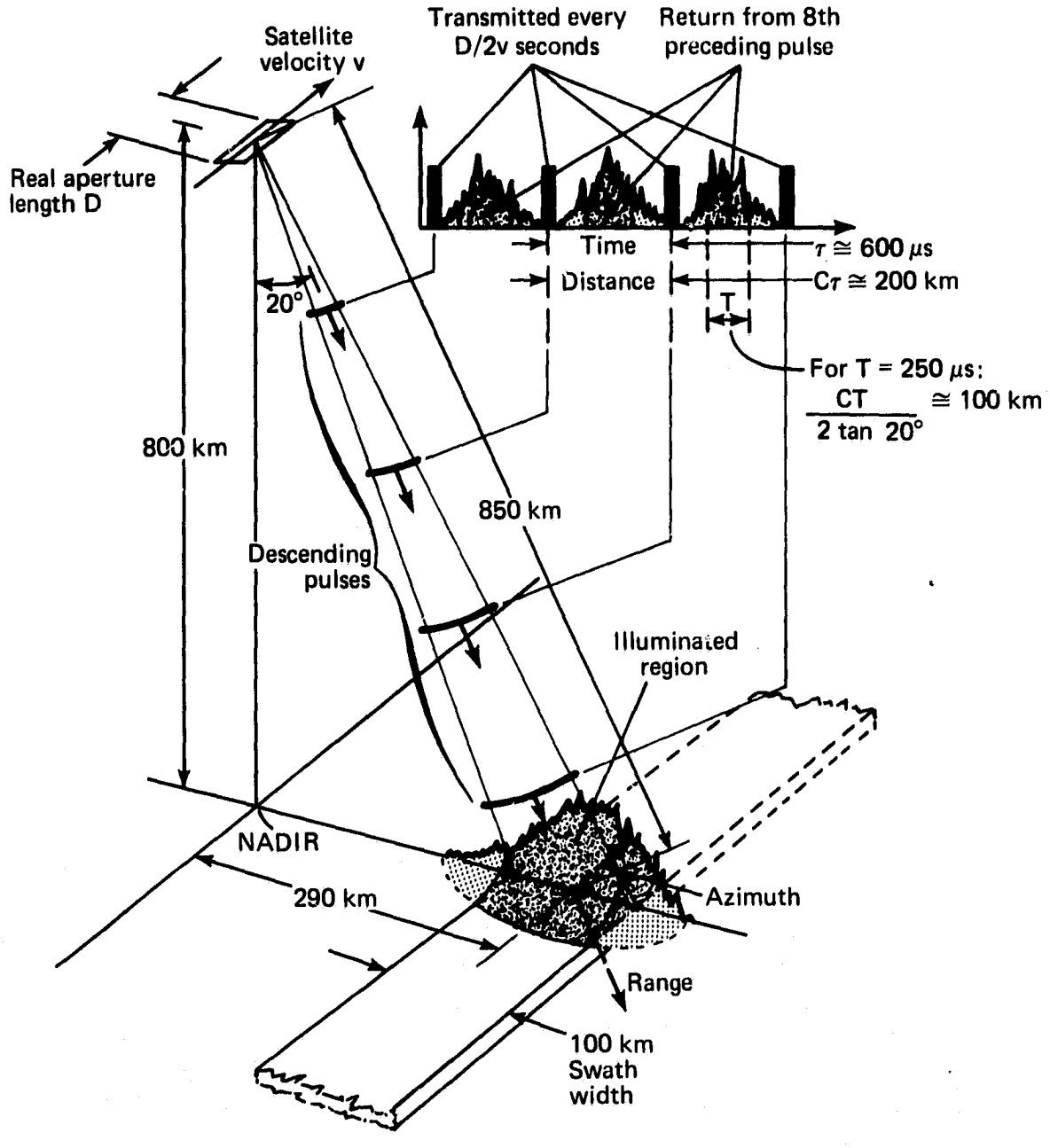

Fig. A3 Synchronization constraints in the SEASAT SAR.

middle 250 μs of return represents a swath width of about 100 km for the Seasat geometry. It is particularly significant that large swaths inherently require very long real apertures, thus increasing the time necessary to collect information from large range differences, while still allowing the synthetic aperture to be properly filled. This is one of the more serious limitations in spaceborne SAR's.

IV. THE NINETY-EIGHT DAY SAR EXPERIMENT

On July 4, 1978, approximately one week after the satellite was launched, the SAR was successfully operated over the Goldstone tracking station. On October 10, as it was passing over the horizon of the United Kingdom station at Oak Hanger, the entire satellite experienced a premature death due to a power system failure. In the ninety-eight days during which the SAR was operating, nearly 500 high density digital tapes were collected at three domestic and two foreign stations. Several months later, only a small percentage of the tapes had been converted to imagery. It is now clear from that small percentage, however, that the remaining tapes contain a wealth of imagery that will take several years to fully analyze and assess.

Because of the relative uncertainty of the ultimate application for spaceborne SAR (i.e., that application for which some user agency is willing to pay), the validation experiments vary widely in content. They all have one thing in common, however. A proper validation experiment, of which there are approximately 30 with the Seasat SAR, must be a comparison between the SAR and some more direct (or in situ) measurement of a common quantity. Typical physical parameters of interest in the SAR experiments are ocean wavelength and direction, ice age and thickness, soil moisture content, and mean surface roughness of geological features.

A properly conducted validation experiment requires not only extensive preparation, but a knowledge of where the satellite will be on a particular date. Unlike the other sensors, the Seasat SAR produced considerable drain on the satellite power system, and was therefore limited to only one hour of pre-programmed operation per day. In fact, for the first two weeks of September, spacecraft problems limited total SAR operation to only ten minutes per day. Throughout the life of the experiment, it was always a challenge for an individual investigator to know when the SAR would be over his particular site, and to insure that

it would be activated at the proper time. Fortunately, a close cooperation between the investigators and Project personnel made possible what could easily have become impossible. In one extreme case, a whole team of people conducting a soil moisture experiment were transferred from one state to another with their instrumentation overnight. Flexibility was a clear attribute.

Figure A-4 is a sequence of the SAR coverage for each week during its lifetime. The five circles are the 10^{o} elevation masks for each of the three domestic and two foreign stations. The largest number of passes was recorded at Goldstone, California, but nearly as many were recorded at Fairbanks, Alaska, and Merritt Island, Florida. Because of a lag in international agreement, the two foreign stations were not initially equipped to receive data. The European station began recording during the sixth week, the Canadian during the ninth. Just as the Canadians were beginning to record data routinely, the spacecraft developed a thermal problem, and SAR operation was significantly curtailed from the tenth through twelfth week. During the tenth week, however, the satellite was placed in a "three-day-repeat" orbit to permit altimeter calibration over Bermuda. This repeating orbit caused the satellite to pass over exactly the same subpoints at three day plus 12 minute intervals, and greatly facilitated the planning of validation experiments. By the thirteenth week, which was the middle of September, the ten-minute-per-day operating limit had been lifted, the orbit was well defined and repeating, and all five stations were receiving comparable quantities of data. This blissful situation continued for slightly more than three weeks, until the satellite's demise at the beginning of the sixteenth week. At the termination of its life, the altimeter had been fully calibrated, and the satellite was scheduled momentarily to be placed into a "baseline" orbit, which would have allowed the instrument subtracks to progress slowly to the east, at a rate of approximately 10 km every three days.

In spite of the early extinction of the satellite and the various obstacles to planning cited above, a surprising number

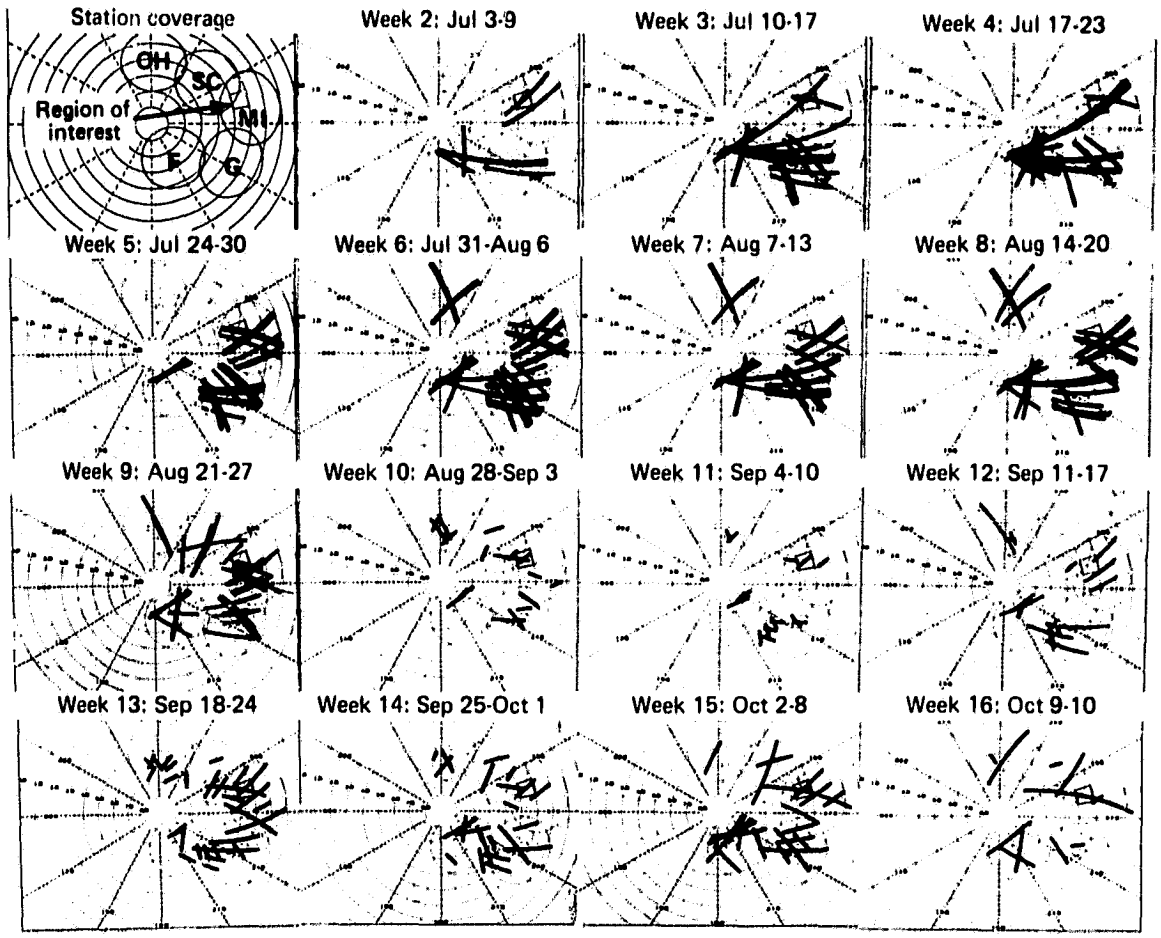

Fig. A-4 Weekly history of SAR coverage, for each of the five stations
Code: OH = Oak Hanger, England
SC = Shoe Cove, Newfoundland
MI = Merritt Island, Florida
G = Goldstone, California
F = Fairbanks, Alaska

of validation experiments were successfully carried out, beginning around the middle of August. One of the more comprehensive experiments was organized by NOAA in the Gulf of Alaska (under the acronym of GOASEX, for Gulf of Alaska Surface Experiment), involving several government organizations and universities. GOASEX was specifically designed to collect the necessary "surface truth" to assist validation of the wind and wave measurement capabilities of each of the spacecraft sensors. Two GOASEX workshops have been held this year (the first in January, the second in June), and significant results for each of the instruments will begin to appear in the literature in the coming months. Several other experiments, including a joint U.S./Canadian ice dynamics study, are currently in various stages of analysis.